The Astrophysical Journal, 871:240 (23pp), 2019 February 1 https://doi.org/10.3847/1538-4357/aafb77

The Accretion History of AGNs. I. Supermassive Black Hole Population Synthesis Model

Tonima Tasnim Ananna[1,2], Ezequiel Treister[3], C. Megan Urry[1,2,4], C. Ricci[5,6,7], Allison Kirkpatrick[1,2], Stephanie LaMassa[8], Johannes Buchner[3,9], Francesca Civano[10], Michael Tremmel[1,2], and Stefano Marchesi[11]
[1] Department of Physics, Yale University, P.O. BOX 201820, New Haven, CT 06520-8120, USA; tonimatasnim.ananna@yale.edu
[2] Yale Center for Astronomy and Astrophysics, P.O. Box 208120, New Haven, CT 06520, USA
[3] Instituto de Astrofísica, Facultad de Física, Pontificia Universidad Católica de Chile, Casilla 306, Santiago 22, Chile
[4] Department of Astronomy, Yale University, P.O. Box 208101, New Haven, CT 06520, USA
[5] Núcleo de Astronomía de la Facultad de Ingeniería, Universidad Diego Portales, Av. Ejército Libertador 441, Santiago, Chile
[6] Kavli Institute for Astronomy and Astrophysics, Peking University, Beijing 100871, People's Republic of China
[7] Chinese Academy of Sciences South America Center for Astronomy and China-Chile Joint Center for Astronomy, Camino El Observatorio 1515, Las Condes, Santiago, Chile
[8] Space Telescope Science Institute, 3700 San Martin Drive, Baltimore, MD 21218, USA
[9] Millennium Institute of Astrophysics, Vicuña. MacKenna 4860, 7820436 Macul, Santiago, Chile
[10] Harvard-Smithsonian Center for Astrophysics, 60 Garden Street, Cambridge, MA 02138, USA
[11] Department of Physics and Astronomy, Clemson University, Kinard Lab of Physics, Clemson, SC 29634, USA
Received 2018 August 21; revised 2018 December 4; accepted 2018 December 8; published 2019 February 5

Abstract

As matter accretes onto the central supermassive black holes in active galactic nuclei (AGNs), X-rays are emitted. We present a population synthesis model that accounts for the summed X-ray emission from growing black holes; modulo the efficiency of converting mass to X-rays, this is effectively a record of the accreted mass. We need this population synthesis model to reproduce observed constraints from X-ray surveys: the X-ray number counts, the observed fraction of Compton-thick AGNs [$\log(N_{\rm H}/{\rm cm}^{-2}) > 24$], and the spectrum of the cosmic X-ray background (CXB), after accounting for selection biases. Over the past decade, X-ray surveys by *XMM-Newton*, *Chandra*, *NuSTAR*, and *Swift*-BAT have provided greatly improved observational constraints. We find that no existing X-ray luminosity function (XLF) consistently reproduces all these observations. We take the uncertainty in AGN spectra into account and use a neural network to compute an XLF that fits all observed constraints, including observed Compton-thick number counts and fractions. This new population synthesis model suggests that, intrinsically, $50\% \pm 9\%$ ($56\% \pm 7\%$) of all AGNs within $z \simeq 0.1$ (1.0) are Compton-thick.

Key words: galaxies: active – Galaxy: center – Galaxy: evolution – methods: data analysis – quasars: supermassive black holes – X-rays: diffuse background

1. Introduction

Supermassive black holes (SMBHs) are found at the cores of most galaxies, and their masses correlate closely with the host bulge mass, velocity dispersion, and luminosity (Magorrian et al. 1998; Richstone et al. 1998; Gebhardt et al. 2000; Kormendy & Gebhardt 2001; Merritt & Ferrarese 2001; Ferrarese & Ford 2005; Kormendy & Ho 2013). This suggests that SMBHs may regulate star formation rates, e.g., through molecular and ionized wind mass outflows (Ferrarese & Merritt 2000; Gebhardt et al. 2000; Di Matteo et al. 2005; Merloni et al. 2010; Fiore et al. 2017; Martín-Navarro et al. 2018). If so, the accretion history of SMBHs has important implications for the evolution of galaxies.

The growth of SMBHs over cosmic time can be traced through the light emitted during rapid growth phases, when the galaxy appears as an active galactic nucleus (AGN). A population synthesis model describes the number density of AGNs as a function of their luminosity and redshift (X-ray luminosity function (XLF)); together with the spectral energy distributions, this model describes all the radiation produced by SMBH growth throughout the universe.

High-energy X-rays are a prime tracer of AGNs because they are produced close to the black hole and they can penetrate all but the thickest columns of absorbing material (Brandt & Hasinger 2005; Cardamone et al. 2008; Donley et al. 2012; Mendez et al. 2013; Kirkpatrick et al. 2015; Del Moro et al. 2016). Additionally, X-ray surveys detect mostly active galaxies rather than inactive galaxies. Therefore, X-rays have the advantage of both sensitivity to obscured AGNs and efficiency of detecting AGNs. Hard X-ray bands are especially important for heavily obscured Compton-thick objects (with column densities $N_{\rm H} > 10^{24}\,{\rm cm}^{-2}$), as well as obscured Compton-thin sources ($N_{\rm H} = 10^{22}$–$10^{24}\ {\rm cm}^{-2}$). Indeed, the number density of heavily obscured objects was one of the most uncertain parts of early population synthesis models because the first X-ray surveys were fairly soft (Maccacaro et al. 1991; Boyle et al. 1993; Comastri et al. 1995; Jones et al. 1997; Page et al. 1997; Miyaji et al. 2000; Gilli et al. 2001). As higher-energy X-ray data (>3 keV) became available (Boyle & Terlevich 1998; Cowie et al. 2003; Ueda et al. 2003, 2014; Gilli et al. 2007; Treister et al. 2009; Aird et al. 2015; Buchner et al. 2015), more obscured AGNs were included.

At this point, there exists a large ensemble of broadband X-ray surveys with different combinations of depth and volume, collectively spanning an extensive range in luminosity and redshift (which in any one flux-limited survey are strongly correlated). In particular, the *Chandra X-Ray Observatory* (Weisskopf et al. 2002) has contributed the Chandra Deep Field South (CDFS) 7 Ms catalog (Luo et al. 2017), which reaches the faintest fluxes at $E < 10\,{\rm keV}$; extended CDFS (Lehmer et al. 2012; Xue et al. 2012; Luo et al. 2017); COSMOS (Elvis et al. 2009); ChaMP (Kim et al. 2007); and Stripe 82X (LaMassa et al. 2013a, 2013b, 2016; Ananna et al. 2017). The *XMM-Newton* observatory has a slightly harder response function than *Chandra* and has also carried out both deep and wide surveys, including *XMM*-CDFS (Ranalli et al. 2013), *XMM*-COSMOS (Cappelluti et al. 2007),

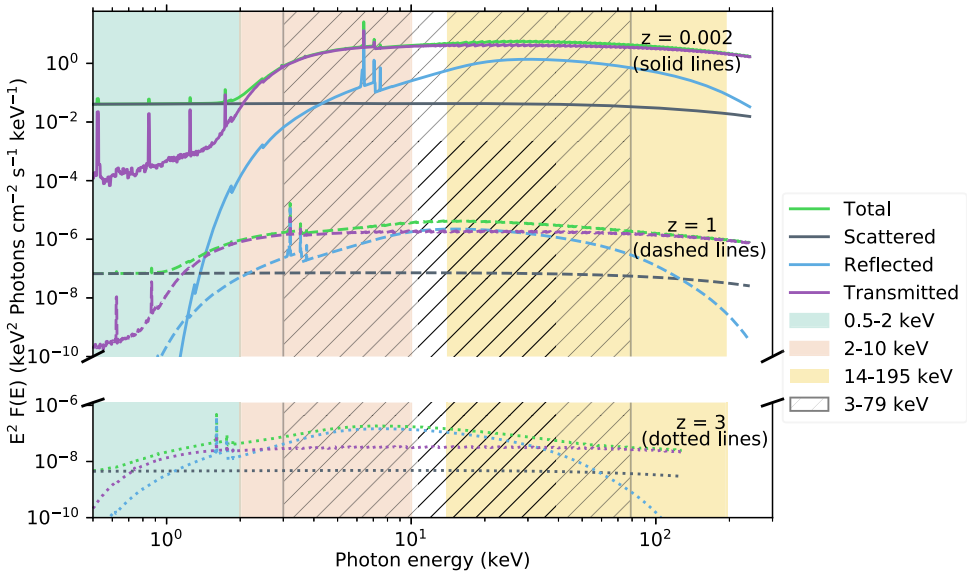

Figure 1. Observed-frame spectra with intrinsic $L_{2-10} = 10^{44}$ erg s^{-1}, log $(N_{\rm H}/{\rm cm}^{-2}) = 23$ at $z = 0.002$ (solid lines) and $z = 1$ (dashed lines) in the top panel and $z = 3$ (dotted lines) in the bottom panel. The plot shows the unabsorbed component scattered by gas outside the torus region (dark-gray lines), the reflection component (light-blue lines) from the accretion disk, transmitted emission (purple lines) from the torus, the total AGN spectra (light-green lines), and the window of observation in typical energy bands. *Chandra* observes in the 0.5–8 keV band, and *XMM-Newton* observes in the 0.5–10 keV band, *Swift*-BAT in the 14−195 keV band, and *NuSTAR* in the 3–79 keV band at this redshift. At $z = 1.0$, the observed flux is six orders of magnitude lower than in the local universe owing to distance, while redshifting allows the instruments to probe higher rest-frame energy bands. The *Chandra* and *XMM* hard bands and, to a larger extent, *NuSTAR* play a vital role in quantifying the strength of the reflection component.

2XMMi (Mateos et al. 2008), Stripe 82X (LaMassa et al. 2013a, 2016), and *XMM*-XXL (Pierre et al. 2016).

At still higher X-ray energies, both the *Neil Gehrels Swift Observatory* Burst Alert Telescope (BAT; 14–195 keV; Gehrels et al. 2004; Barthelmy et al. 2005) and *NuSTAR* (3–79 keV; Harrison et al. 2013) have contributed the most unbiased surveys to date. *Swift*-BAT and *NuSTAR* are particularly sensitive to heavily obscured AGNs, as higher-energy X-ray photons are less susceptible to absorption. *Swift*-BAT is a nonfocusing X-ray observatory that images the sky in five bands between 14 and 195 keV (Barthelmy et al. 2005). *NuSTAR* observes in a lower-energy band (3–79 keV) and is the first orbiting telescope that focuses X-ray light above 10 keV, increasing its sensitivity by two orders of magnitude.

In this work, we show that existing XLFs cannot explain the X-ray data observed in all these new surveys. We explore the uncertainty in AGN X-ray spectra and, using a neural network, find an XLF that satisfies all observed constraints. Those constraints include the integrated spectrum of the cosmic X-ray background (CXB), the overall X-ray number counts (i.e., the number of AGNs observed per unit area of the sky as a function of flux), and the Compton-thick AGN number counts and fraction in each survey.

Our new population synthesis model is presented as follows: The X-ray spectra of AGNs are discussed in Section 2. The most recent XLFs are described in Section 3. The observational constraints from X-ray surveys are discussed in Section 4. Our approach of formulating a new population synthesis model is described in Section 5. Our results are presented in Section 6. The conclusions and summary of this work are presented in Sections 7 and 8, respectively.

2. AGN X-Ray Spectra

In this work, we focus on the light emitted in X-ray bands as SMBHs grow. Understanding AGN X-ray spectra is necessary to interpret observed X-ray samples and to constrain the population synthesis model. Figure 1 shows the X-ray spectra of a moderately obscured AGN at three different redshifts while keeping all other spectral parameters constant. It also shows energy windows of *Chandra* and *XMM-Newton* (<10 keV), *NuSTAR* (8–24 keV), and *Swift*-BAT (14–195 keV) X-ray instruments.

The AGN X-ray spectrum affects the conversion between number counts and flux, as well as the sensitive area of each survey. The origin of the X-ray spectra (shown in Figures 2–4) is the hot corona around the accretion disk, and the shape of the spectrum is a power law, with a photon index in the range $\Gamma \simeq 1.4$–2.1 (Nandra & Pounds 1994; Ueda et al. 2014; Ricci et al. 2017) and an exponential cutoff energy, i.e., $F(E) \propto E^{-\Gamma} \exp(-E/E_{\rm cutoff})$. This emission is reflected by the accretion disk, which is <1 pc from the central SMBH (Nenkova et al. 2002; Jiménez-Vicente et al. 2014), and reprocessed by a torus-like distribution of obscuring material ≃10–100 pc from the AGN (Nenkova et al. 2002). The torus absorbs optical, ultraviolet, and X-ray photons and reemits it in infrared. The unabsorbed continuum can be scattered by gas outside the torus region. The Fe Kα emission line at around 6.4 keV is prominent in AGN spectra and is thought to have originated either in the outer regions of the accretion disk or in the inner region of the torus (Nandra 2006).

Each of these components has to be modeled in order to calculate observable quantities, such as CXB. For this work, each component was modeled using XSPEC (Arnaud 1996). The Compton reflection from the accretion disk is modeled using the PEXRAV (Magdziarz & Zdziarski 1995) or PEXMON (Nandra et al. 2007) model, where the latter updates the former with self-consistent Fe Kα emission lines relative to the power law. Torus models such as BNTORUS (Brightman & Nandra 2011) self-consistently account for transmitted power law, reflection, and fluorescence lines from metals. The Thomson-scattered component, from ionized material within the torus

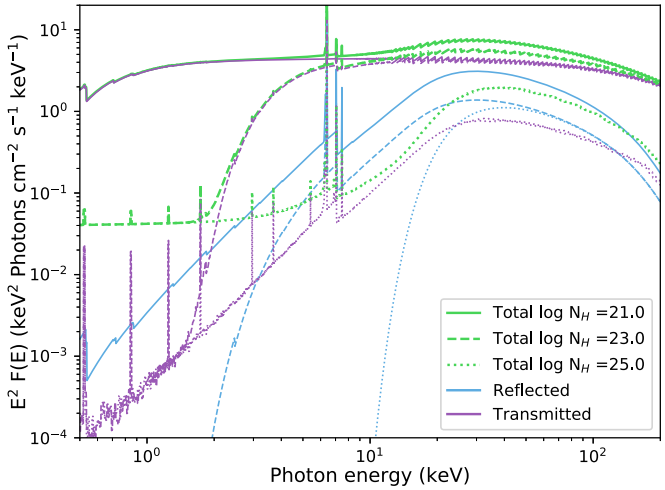

Figure 2. Variation in X-ray spectra with absorbing column density $\log(N_{\rm H}/{\rm cm}^{-2})$, where column density varies from $\log(N_{\rm H}/{\rm cm}^{-2}) = 21$ (solid lines) to $\log(N_{\rm H}/{\rm cm}^{-2}) = 23$ (dashed lines) to $\log(N_{\rm H}/{\rm cm}^{-2}) = 25$ (dotted lines). The components are reflection (blue lines) from the accretion disk, reprocessed emission (purple lines) from the torus, and the sum of all components (green lines). The scattered component is not shown for clarity. Spectral parameters other than absorption are fixed at $\Gamma = 1.96$, $R = 0.83$ for unabsorbed and $R = 0.37$ for absorbed sources, $E_{\rm C} = 200$ keV, and $f_{\rm scatt} = 1\%$.

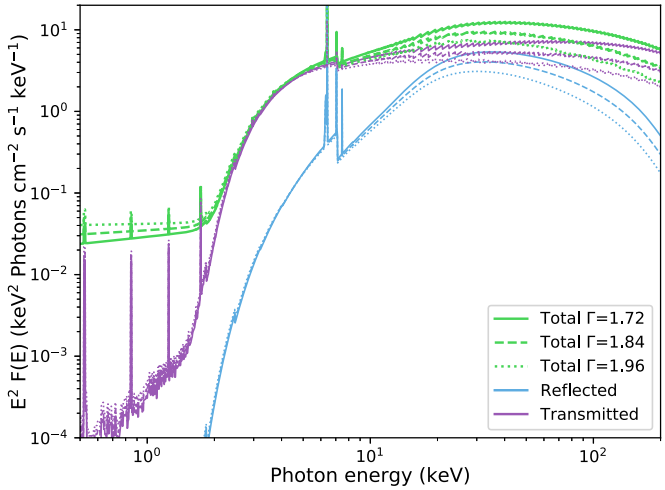

Figure 3. Variation in X-ray spectra with photon index Γ, where Γ is varied from 1.72 (solid lines) to 1.84 (dashed lines) to 1.96 (dotted lines). The components are reflection (blue lines) from the accretion disk, reprocessed emission (purple lines) from the torus, and the sum of all components (green lines). The scattered component is not shown for clarity. Spectral parameters other than Γ are fixed at a constant scattering fraction ($f_{\rm scatt} = 1\%$), cutoff energy ($E_{\rm C} = 200$ keV), absorbing column density ($\log(N_{\rm H}/{\rm cm}^{-2}) = 23$), and reflection scaling factor ($R = 0.83$).

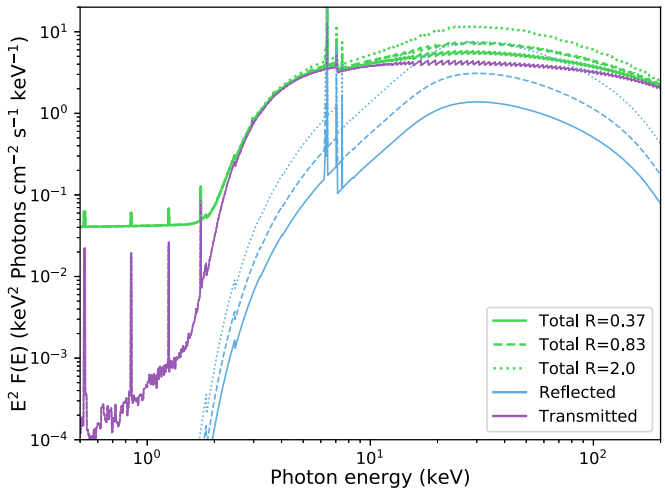

Figure 4. Variation in X-ray spectra with reflection scaling factor R, where R is varied from 0.37 (solid lines), 0.83 (dashed lines), to 2 (dotted lines). The components are reflection (blue lines) from the accretion disk, reprocessed emission (purple lines) from the torus, and the sum of all components (green lines). The scattered component is not shown for clarity. Spectral parameters other than reflection scaling factor are fixed at $\Gamma = 1.96$, cutoff energy $E_{\rm C} = 200$ keV, $\log(N_{\rm H}/{\rm cm}^{-2}) = 23$, and $f_{\rm scatt} = 1\%$.

opening angle, has the same shape as the power law and some fraction ($f_{\rm scatt}$) of its magnitude. This component dominates at $E < 2$ keV, as shown in Figure 1.

Buchner et al. (2015) show that the sum of torus, PEXMON, and scattering is currently the best prescription to model AGN spectra. A second-order effect that could slightly modify the spectra is a Compton scattering of the PEXMON component, which itself is a neutral Compton reflection from the accretion disk, by the compact torus. A multiplicative XSPEC model that downscatters photons for a Compton-thick obscurer is not currently available. However, this effect is likely to be marginal compared to the uncertainty due to the range of reflection scaling factors used in the literature.

Figure 2 demonstrates the effects of obscuration on AGN spectra by varying levels of equivalent hydrogen atom column density ($N_{\rm H}/{\rm cm}^{-2}$). We can see that at $E < 10$ keV, a Compton-thin obscuring column density of $\log(N_{\rm H}/{\rm cm}^{-2}) = 23$ can significantly decrease the observed fluxes, especially in the soft band where the total $E^2\ F(E)$ drops by almost two orders of magnitude. For this reason, heavily obscured Compton-thin and Compton-thick objects are difficult to observe in the local universe using $E < 10$ keV bands, and the higher-energy bands from *NuSTAR* and *Swift*-BAT are required at $z < 1$. At higher redshifts, the spectrum gets shifted to lower-energy bands (as shown in Figure 1) and can be detected at observed frame $E < 10$ keV.

The contribution to the CXB by objects in each $N_{\rm H}$ bin distinctly shapes the overall CXB spectrum because of the way obscuration affects AGN spectra, as shown in Figure 2. Even with a high reflection scaling factor of $R = 0.83$, the unabsorbed spectrum is relatively flat. If the CXB were dominated by unabsorbed objects with $\log(N_{\rm H}/{\rm cm}^{-2}) < 22$, it should have a shape similar to an unabsorbed AGN spectra. Similarly, a Compton-thin-dominated CXB should be low at <2 keV but rise and become approximately flat until 60–70 keV, depending on the cutoff energy of the intrinsic power law. A substantial contribution from Compton-thick objects will produce the characteristic peak (Compton hump) at 20–30 keV that we observe in the CXB, similar to the spectrum of a Compton-thick object.

Figures 3 and 4 provide some insight into how the spectrum varies owing to variation in photon index and reflection scaling factor, which in turn helps us understand how this affects the CXB. These figures show the reflected and the transmitted components of the AGN spectra (the scattered component does not vary greatly, so it is removed from the figures for clarity) and the sum of all components. Figure 3 shows that higher Γ causes steeper decline at $E > 10$ keV. Figure 4 shows how the reflection component changes with reflection scaling factor R,

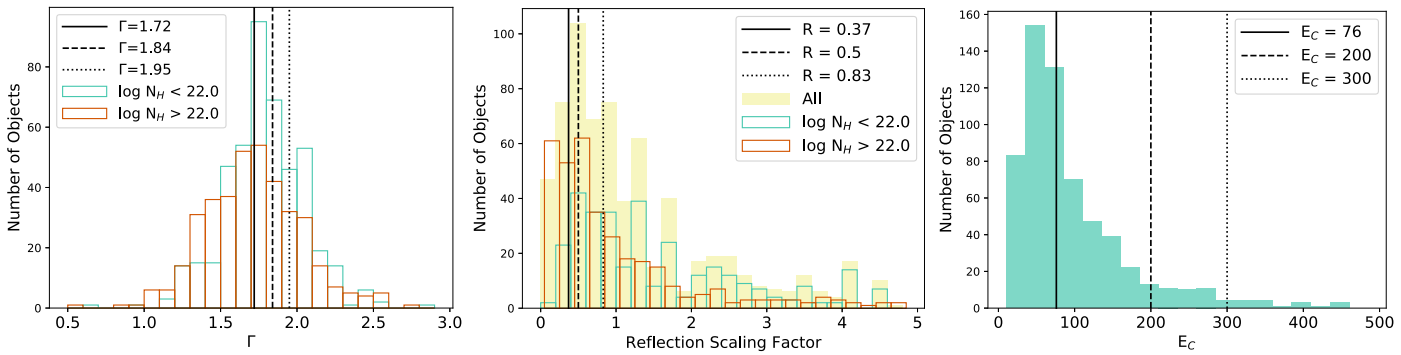

Figure 5. AGN power-law spectral photon index (left), reflection scaling factor (middle), and cutoff energy (right) distributions for the *Swift*-BAT 70-month sample (Ricci et al. 2017). In the left and middle panels, the unabsorbed and absorbed population Γ distributions are plotted in two distinct histograms, log $(N_{\rm H}/{\rm cm}^{-2}) < 22$ (light green) and log $(N_{\rm H}/{\rm cm}^{-2}) > 22$ (orange). Most of the reflection scaling factor values are upper limits, whereas most of the cutoff energy values are lower limits. Ueda et al. (2014) parameter values are indicated by black solid and dashed vertical lines in the left and middle panels. In the right panel, the U14 cutoff energy, $E_{\rm C} = 300$ keV, is shown with the dotted line, and the *Swift*-BAT 70-month observed median ($E_{\rm C} = 76$ keV) and bias-corrected median ($E_{\rm C} = 200$ keV) are shown with solid and dashed lines, respectively.

with a more prominent bump for stronger reflection. Thus, a high R value, rather than a large number of obscured sources, can also cause the prominent bump; however, spectral fitting of *Swift*-BAT and *NuSTAR* sources shows that R generally lies below 1 (Ricci et al. 2017; Zappacosta et al. 2018).

2.1. Observed AGN Spectra

Ricci et al. (2017) presented a detailed X-ray spectral analysis of AGNs of the local universe. This analysis was carried out using *Swift*-XRT (Burrows et al. 2005; Moretti et al. 2009), *XMM-Newton*, and *Chandra* data for $E < 10$ keV and *Swift*-BAT data in 14–150 keV for 836 sources in the local universe (85% of the sources are at $z < 0.1$). The wide wavelength coverage, large sample size, and relatively unbiased data make the parameter distribution from this sample a robust empirical measure of X-ray spectral parameters. Ricci et al. (2017) report that a Kolmogorov–Smirnov (K-S) test between the distributions of photon indices of unobscured and obscured sources shows that the two distributions are significantly different. Fitting a Gaussian to the photon indices of unobscured AGNs yields $\langle\Gamma\rangle \simeq 1.8$ and $\sigma_\Gamma = 0.24$, higher than those of obscured AGNs: $\langle\Gamma\rangle \simeq 1.72$ and $\sigma_\Gamma = 0.31$. Tueller et al. (2008), Burlon et al. (2011), Ueda et al. (2014), and Zdziarski et al. (2000) also find a higher photon index for unobscured sources compared to obscured sources.

Ricci et al. (2017) report that the reflection scaling factor R varies significantly based on obscuration: $R_{\rm median} = 0.83 \pm 0.14$ for unobscured sources and $R_{\rm median} = 0.37 \pm 0.11$ for obscured sources. We performed a K-S test on the cutoff energy parameter of the AGN power law for obscured and unobscured objects but did not find a statistically significant difference between the two distributions (p-value $= 0.42$). The cutoff energy was well constrained for 161 sources. The median cutoff energy found by *Swift*-BAT for these 161 objects is 76 keV, and most of these energies are below 100 keV. The overall distributions of these three parameters are shown in Figure 5.

Swift-BAT covers the widest wave band, but the BAT sample is at low redshifts: 85% of the sample is below $z = 0.1$. Spectral fitting is also susceptible to biases: Ricci et al. (2017) report that cutoff energies in the *Swift*-BAT 70-month survey data can only be constrained for sources where this value lies below 100 keV, and reflection parameters are easier to constrain when this value is large. Even though the median of all *observed* cutoff energy values is 76 keV, a Kaplan−Meier estimator on these energy values, including all the lower limits, yields a median value of 200 ± 29 keV. Additionally, spectral parameters may be coupled. Zdziarski et al. (1999) and Petrucci et al. (2001) report a correlation between reflection parameter and photon index, whereas Matt (2001) report a positive correlation between photon index and cutoff energies. These correlations may occur as a result of the intrinsic nature of the spectra, or the fact that they are strongly related in the fitting procedure. Similarly, the difference of observed parameters between obscured and unobscured sources might be intrinsic but can also arise owing to imperfections in the modeling of the obscurer (Baloković et al. 2018).

Ueda et al. (2014) fit 14–195 keV spectra of *Swift*-BAT 9-month catalog sources with a power-law model, with fixed reflection parameter ($R = 0.5$) and cutoff energy (300 keV), and derived photon indices of $\langle\Gamma\rangle = 1.84$ for obscured sources and $\langle\Gamma\rangle = 1.94$ for unobscured sources. Nandra & Pounds (1994) reported $\Gamma = 1.9-2.0$, assuming power-law spectra without a cutoff energy. Ricci et al. (2017) also find a $\langle\Gamma\rangle$ value consistent with these results by fitting 14−195 keV data with a simple power-law model ($\langle\Gamma_{\rm BAT}\rangle = 1.96$), even though the $\langle\Gamma\rangle$ for overall broadband spectral fitting is lower (i.e., $\langle\Gamma\rangle = 1.72$ for obscured sources and $\langle\Gamma\rangle = 1.80$ for unobscured sources).

The predicted CXB and number counts from any XLF vary depending on the assumed spectra. The consequence of spectral parameter uncertainties on observed constraints is explored further in Sections 5 and 6.

2.2. Modeled AGN Spectra in Existing Population Synthesis Models

Here we describe the AGN spectra of the three population synthesis models examined in this paper. The main spectral parameters are summarized in Table 1. The XLFs of these models are discussed in more detail in Section 3. Ueda et al. (2014, hereafter U14) assume constant $\Gamma \simeq 1.84$ and 1.94 for obscured and unobscured sources, respectively, a reflection scaling factor of $R = 0.5$, based on the averaged reflection strength of local Seyfert galaxies, modeled using PEXRAV. For the torus component, U14 uses BNTORUS, where the opening angle of the torus is related to the fraction of absorbed AGNs. The scattering component is dependent on the torus opening angle $\propto(1–\cos\theta_{\rm OA})$. The cutoff energies of these spectra are assumed to be 300 keV.

Table 1
Summary of X-Ray Spectral Parameters in Recent Population Synthesis Models and Observations

Model/Observation	Photon Index $\langle\Gamma\rangle$	Refl. Scaling Factor (R)	$E_{\rm cutoff}$ (keV)	$f_{\rm scatt}$
Ricci et al. (2017)[a]	1.72 (obscur), 1.8 (unobsc)	0.37 (obscur), 0.83 (unobsc)	76[b]	≃1%
Ueda et al. (2014)[c]	1.84 (obsc), 1.94 (unobsc)	0.5	300	≃1%
Aird et al. (2015)[c]	1.9	0–2. (uniform)	300	≃1%
Buchner et al. (2015)[c]	1.95	0.1–2. (log uniform)	No cutoff	≃1%

Notes.
[a] Observed parameters determined by detailed X-ray spectral fittings to *Swift*-BAT 70-month survey sources.
[b] The cutoff energies measured in *Swift*-BAT can only be adequately constrained when the value is lower than 100 keV.
[c] Parameter values assumed to model X-ray spectra for each respective X-ray luminosity function.

The same three spectral components are used in the Aird et al. (2015, hereafter A15) AGN template spectra as well. The photon index is modeled by a normal distribution with $\langle\Gamma\rangle = 1.9$ and $\sigma_\Gamma = 0.2$. The reflection scaling factor is drawn from a uniform distribution between 0 and 2.0, and the scattering fraction is of the order of 1%, drawn from a lognormal distribution. The cutoff energy is assumed to be 300 keV as well.

Buchner et al. (2014) presented a Bayesian analysis of spectra of ≃350 AGNs from the 4 Ms CDFS. The most probable model is similar to the U14 model, in that it also has scattering, reflection, and torus components. A power law is assumed as the intrinsic spectrum, but without any cutoff energies. The reflected component is modeled with PEXMON instead of PEXRAV (which was used by U14), and the transmitted component was modeled using BNTORUS. Buchner et al. (2015, hereafter B15) use this spectrum in their population synthesis model. The scattering component is independent of opening angle and is allowed to vary uniformly between 0.0001 and 0.1 in log space. The photon index can vary within a Gaussian distribution with $\langle\Gamma\rangle = 1.95$ and $\sigma_\Gamma = 0.15$, and the reflection scaling factor R is drawn from a log uniform distribution in the range of 0.1–2.

We compared the distributions used in previous population synthesis models with the parameters observed in *Swift*-BAT 70-month survey spectra. Figure 5 shows the observed distribution plotted against suggested values for U14 spectra (A15 and B15 uses a distribution for these parameters with $\langle\Gamma\rangle$ close to the dotted line). The Γ is slightly higher than observed values for all the models, but the most noticeable difference is the cutoff energy, which is much higher for the models. Note that if observational biases are taken into account, the cutoff energy is estimated to be higher (200 keV; Ricci et al. 2017).

3. A Brief Review of XLFs

Early XLFs were based on soft X-ray bands (Maccacaro et al. 1991; Boyle et al. 1993; Jones et al. 1997; Page et al. 1997; Miyaji et al. 2000). One of the first hard XLFs, Ueda et al. (2003), introduced an "absorption function" as part of the XLF, which takes into account what fraction of objects at each luminosity and redshift falls in each $N_{\rm H}$ bin. This addition meant that the spectrum of an AGN can be corrected in the rest frame for absorption effects. This is important in hard XLFs, which include more absorbed AGNs. The population synthesis model of Ueda et al. (2003) defined the following three components: (i) an AGN template spectrum, the shape and normalization of which vary with $N_{\rm H}$ and intrinsic rest-frame luminosity (L_{2-10}), respectively, as described in Section 2; (ii) a distribution of how space density varies with L_{2-10} and z; and (iii) an absorption function of how this space density is distributed in $N_{\rm H}$ bins. The second component, the space density per comoving Mpc^3, follows a double power-law relationship as a function of luminosity (as shown in Equation (11) in Ueda et al. 2003 and Equation (14) in Ueda et al. 2014). The second and third components of population synthesis models can be dependent on each other, so the most general XLFs give space densities based on all three parameters (z, L_{2-10}, $N_{\rm H}$).

Most recent population synthesis models provide the same three components (spectrum, XLF, and $N_{\rm H}$ distribution), although the form of the function is sometimes different (Aird et al. 2010, 2015), or the AGN spectrum has different components or a different distribution of spectral parameters. We discuss three of the most recent XLFs in this section, which were formulated using the most recent surveys with the most representative samples of AGNs. We consider these three models when fitting all the latest observed constraints.

3.1. Ueda et al. (2014)

U14 used a maximum likelihood method to fit a double power-law luminosity function for the local universe and a redshift evolution function, which together follow a complex luminosity-dependent density evolution (LDDE) relationship. The AGN samples used to derive the XLF are selected in 0.5–195 keV in X-ray bands and have high identification completeness (⩾90%).

Even though all available samples are used to formulate the XLF, to construct a robust absorption function, U14 only uses samples with the highest photon counts: the *Swift*-BAT 9-month survey (Tueller et al. 2008), *ASCA* Medium Sensitivity Survey (AMSS; Ueda et al. 2001; Akiyama et al. 2003), and Subaru/*XMM-Newton* Deep Survey (SXDS; Ueda et al. 2008) data. *Swift*-BAT data were used to quantify the local absorption function, and AMSS and SXDS data were used to formulate the redshift/luminosity evolution. *XMM-Newton* and *Chandra* sources were not used to constrain the absorption function because the faint flux limits result in too few photons to construct a reliable X-ray spectrum. U14 constrains the absorption function separately from the XLF to avoid strong parameter coupling.

3.2. Buchner et al. (2015)

B15 used a nonparametric approach on ≃2000 AGNs selected in the 2−7 keV band to derive an XLF that does not impose any form on the luminosity function. The final product of this approach are 3D matrices of space densities in z, L_{2-10}, and $\log(N_{\rm H}/{\rm cm}^{-2})$ bins. A thousand equally likely Markov

chain Monte Carlo (MCMC) samples/matrices are generated based on the uncertainties imposed by the data. The Bayesian prior in this approach are two types of smoothness assumptions about how space densities vary from one bin to another: (i) constant value prior and (ii) constant slope prior. The constant value prior requires that the space density from one bin to the next stays constant unless constraints are imposed by the data. The value of a bin scatters around its neighbor's density value following a normal distribution with an allowed correlation width for luminosity and redshift axes. The constant slope prior is only applied to L_{2-10} and log ($N_{\rm H}/{\rm cm}^{-2}$) and requires that the space density follows a constant power-law slope from one bin to the next unless constraints are imposed by the data. The slope scatters around the neighbor's slope following a normal distribution. Each of the two assumptions provides 500 samples, resulting in a total of 1000.

3.3. Aird et al. (2015)

The A15 XLF was formulated using a parametric Bayesian approach. A15 derived XLFs for 0.5–2 keV and 2–7 keV X-ray samples separately and then incorporated absorption effects and modeled the unobscured and obscured samples separately. Consequently, there are two components of the A15 XLF, with different sets of parameters, one for absorbed and one for unabsorbed AGNs. Unlike U14 and B15, A15 does not calculate $N_{\rm H}$ for individual sources. However, their approach statistically predicts an $N_{\rm H}$ distribution by global comparisons between the soft- and hard-band samples. A15 account for contribution from star-forming galaxies to the CXB by formulating a galaxy luminosity function. This contribution should not be ignored when synthesizing the CXB using AGN XLFs.

We briefly summarize these XLFs again when we discuss our approach in this work in Section 5.

4. The Observed Constraints

In Table 2, we list all the observed constraints considered in this work, and we explain each of these constraints in this section. Along with the CXB, we consider AGN number counts and observed Compton-thick fractions. The AGN number counts, i.e., the number of AGNs observed per square degree of the sky at a given flux limit in an X-ray band, should be reproduced by a complete population synthesis model, for surveys of all depths, volumes, and energy ranges.

Every X-ray survey probes some region of L_X, z, and $N_{\rm H}$ space. Typically, large-volume X-ray surveys, such as Stripe 82X (LaMassa et al. 2013a, 2013b, 2016; Ananna et al. 2017) and *XMM*-XXL (Pierre et al. 2016), sample more rare, luminous quasars, whereas deep pencil-beam surveys, such as CDFS (Giacconi et al. 2002; Lehmer et al. 2012; Luo et al. 2017), are sensitive down to very low fluxes but are limited to finding low- to moderate-luminosity AGNs. The CDFS 7 Ms (Luo et al. 2017) catalog is the deepest of X-ray surveys, covering a total area of 484.2 arcmin^2, with 1008 sources detected in the 0.5–7 keV energy range. It has been previously shown that existing luminosity functions reasonably reproduce number counts down to 10^{-15} erg cm^{-2} s^{-1} in this energy range (Ballantyne et al. 2011). The deeper CDFS 7 Ms catalog allows comparison to even fainter fluxes, and our new results are presented in Section 6.

We also include number counts in the 0.5–2 keV and 2–10 keV bands from 2*XMM*i (Mateos et al. 2008), *XMM*-COSMOS (Cappelluti et al. 2007), *Chandra* COSMOS (Elvis et al. 2009), *XMM*-CDFS (Ranalli et al. 2013), and Stripe 82X (LaMassa et al. 2013a, 2013b, 2016; Ananna et al. 2017) and 0.5–2 keV and 2–8 keV number counts from Extended Chandra Deep Field Survey (E-CDFS; Lehmer et al. 2005) and *Chandra* Multi-wavelength Project (ChaMP; Kim et al. 2007). 2*XMM*i is an *XMM-Newton* Serendipitous Survey covering 132.3 deg^2 and contains more than 30,000 objects down to flux limits of 10^{-15} erg cm^{-2} s^{-1} in the 0.5–2 keV bin and 10^{-14} erg cm^{-2} s^{-1} above 2 keV. *XMM*-COSMOS is a 2.13 deg^2 survey with a total exposure time of ∼1.5 Ms, reaching similar flux levels to 2*XMM*i homogeneously for 90% of the total area. *Chandra* COSMOS covers a smaller area in the COSMOS-Legacy field (0.9 deg^2), but with twice the effective exposure time as *XMM*-COSMOS, and reaches nearly 10^{-16} erg cm^{-2} s^{-1} flux levels in both soft and hard bands. ChaMP covers a ∼10 deg^2 area, with the deepest 0.5–8 keV levels reaching 9×10^{-16} erg cm^{-2} s^{-1}, and has a range of exposure times of 0.9–124 Ks. For ease of comparison, we convert all the hard-band *Chandra* and *XMM* surveys to the 2–7 keV band. To convert the harder-band fluxes (2–10 keV and 2–8 keV) to 2–7 keV, we use the photon indices adopted by each survey: $\Gamma = 1.6$ for 2*XMM*i; $\Gamma = 1.7$ for *XMM*-CDFS, *XMM*-COSMOS, Stripe 82X; and $\Gamma = 1.4$ for E-CDFS, *Chandra* COSMOS, and ChaMP.

Heavily obscured Compton-thick sources are one of the biggest remaining uncertainties in population synthesis models. Lanzuisi et al. (2018) provide a careful analysis of *Chandra* COSMOS-Legacy survey spectra to produce Compton-thick number counts in the $0.04 < z < 3.5$ range. We compare these Compton-thick number counts with existing models in Section 6.

At $E > 10$ keV bands, the *Swift*-BAT 70-month catalog provides a hard-X-ray-selected sample in the nearby universe ($z < 0.1$), and *NuSTAR* Extragalactic Surveys provide an equivalent sample up to $z \sim 1$ (Aird et al. 2015; Harrison et al. 2016; Lansbury et al. 2017). We calculate overall number counts of the *Swift*-BAT 70-month catalog presented in Ricci et al. (2017), in the 14–195 keV band. We compare the *Swift*-BAT overall counts, as well as *NuSTAR* Extragalactic Survey overall number counts from Harrison et al. (2016), with existing models. The *NuSTAR* Extragalactic Surveys are a wedding cake survey, and we look at three tiers in this work: UKIDSS Ultra Deep Survey (UDS; Masini et al. 2018), COSMOS (Civano et al. 2015), and Serendipitous Survey (Alexander et al. 2013; Lansbury et al. 2017). The details of each of these surveys are given in Table 2. Masini et al. (2018) find an observed Compton-thick fraction in the UDS field—11.5% ± 2.0%. Civano et al. (2015) calculate the Compton-thick fraction using two objects (out of 91) from the *NuSTAR* COSMOS field. The observed fraction of Compton-thick objects found in this work is between 13% and 20%.

Lansbury et al. (2017) calculated *NuSTAR* band ratios from the Serendipitous Survey to select eight (out of 497) heavily obscured objects with the hardest X-ray spectra. They present an analysis of the soft and hard X-ray properties of these sources (the soft bands provided by *Chandra*, *Swift*-XRT, or *XMM-Newton*), as well as multiwavelength properties. Of these Compton-thick objects (in this case, $N_{\rm H} > 1.5 \times 10^{24}$ cm^{-2}), three are at low redshifts ($z \simeq 0.036$, 0.034, 0.069) and one Compton-thick AGN is at a relatively higher redshift (z ∼0.16). Using these four objects, Lansbury et al. (2017) calculated Compton-thick number counts with a low-redshift bias, an

Table 2
Observed Constraints on AGN Population in X-Ray Band

Constraint	Survey	Band (keV)	Area (deg^2)	Depth (erg cm^{-2} s^{-1})	Number of Sources	References
Integrated X-ray background	*Swift*-BAT	14–195	All sky			Ajello et al. (2008)
	Chandra COSMOS	0.3–7	2.15			Cappelluti et al. (2017)
	RXTE	3–20	22600			Revnivtsev et al. (2003)
	ASCA SIS	2–10	0.14			Gendreau et al. (1995)
Number counts	*NuSTAR* extragal. overall number counts:	8–24			124	Harrison et al. (2016)
	(1) *NuSTAR* COSMOS	8–24	1.7	1.3×10^{-13}	91	Civano et al. (2015)
	(2) *NuSTAR* E-CDFS	8–24	0.3	2.5×10^{-14}	19	Mullaney et al. (2015)
	(3) *NuSTAR* EGS	8–24	0.23	2.5×10^{-14}		J. Aird (2019, in preparation)
	(4) *NuSTAR* Serendipitous Survey	8–24	13	$2–10 \times 10^{-14}$	24	Lansbury et al. (2017)
	NuSTAR Ser. Compton-thick counts and fraction	8–24			4	Lansbury et al. (2017)
	NuSTAR COSMOS Compton-thick fraction	8–24			2	Civano et al. (2015)
	NuSTAR UDS Compton-thick fraction	8–24	0.6	2.7×10^{-14}	6.8 ± 1.2	Masini et al. (2018)
	Swift-BAT 70-month all source counts	14–195	All sky		838	Ricci et al. (2017)
	Chandra Deep Field South 7 Ms	0.5–7	0.1345	2.7×10^{-17}	1008	Luo et al. (2017)
	2*XMM*i	0.5–10	132.3	$\times 10^{-14}$	30,000	Mateos et al. (2008)
	XMM-COSMOS	0.5–10	2.13	7×10^{-16}	1416	Cappelluti et al. (2007)
	Chandra COSMOS	0.5–10	0.5	5.7×10^{-16}	1655	Elvis et al. (2009)
	ChaMP	0.5–8	10	9×10^{-16}	6800	Kim et al. (2007)
	Stripe 82X	0.5–10	31.3	2.1×10^{-15}	6181	LaMassa et al. (2013a, 2013b, 2016)
	XMM-CDFS	2–10	0.1345	6.6×10^{-16}	339	Ranalli et al. (2013)
	Extended CDFS	0.5–8	0.3	6.7×10^{-16}	915	Lehmer et al. (2005)
	Chandra COSMOS Leg. Comp.-thick num counts	2–8			41.9	Lanzuisi et al. (2018)
X-ray luminosity functions	Ueda et al. (2014)	0.5–195				
	Buchner et al. (2015)	2−7				
	Aird et al. (2015)	0.5−7				

upper limit in Compton-thick number counts without any bias, and a Compton-thick fraction. They report a Compton-thick fraction of $\simeq$30% in the local universe ($z < 0.07$).

In Table 2, we list the three luminosity functions we examine in this work as observed constraints as well. Since these luminosity functions were derived from data, they should reasonably agree with each other, as well as any new luminosity function. Each survey and model is a step toward converging on the correct solution, and so we compare luminosity functions against each other to verify whether they are in reasonable agreement. The results of these comparisons are presented in Section 6.

5. New Model

Existing population synthesis models do not reproduce all observed constraints (shown in Section 6), so we attempted to update the existing XLF, which is best fit to the CXB (U14), using a newer absorption function by Ricci et al. (2015, hereafter R15). The R15 absorption function is based on the *Swift*-BAT 70-month sample whereas the U14 function was based on the *Swift*-BAT 9-month sample.

R15 reports a completeness-corrected absorption function for the *Swift*-BAT 70-month survey, based on assumptions about the geometry of the torus component. Specifically, the corrections to the absorption functions are calculated by assuming two different opening angles of the torus component of the AGN, 35° and 60°. These corrections are calculated in two luminosity bins: $\log(L_{14-195}/\mathrm{erg\,s^{-1}}) = 40{-}43.7$ and $\log(L_{14-195}/\mathrm{erg\,s^{-1}}) = 43.7{-}46$. The corrected fractions are shown in Figure 4 of R15 and also in Section 6 of this work.

Both U14 and R15 absorption functions are normalized in the $\log(N_{\rm H}/\mathrm{cm^2}) = 20$–$24$ range. Using *Swift*-BAT 9-month data, U14 quantified the fraction of objects in four equally spaced $\log(N_{\rm H}/\mathrm{cm^2})$ bins in the 20–24 range at a fixed luminosity: $\log(L_{2-10}/\mathrm{erg\,s^{-1}}) = 43.75$. Then, luminosity dependence and redshift dependence were added to these fractions based on observed relationships. U14 assumes that the number of Compton-thin objects is equal to the number of Compton-thick objects at any redshift and luminosity bin, and evenly divided over the $\log(N_{\rm H}/\mathrm{cm^2}) = 24$–$26$ bin.

As U14 underestimates Compton-thick number counts, we updated it with the R15 absorption function with the higher Compton-thick fractions: the correction that assumes a torus opening angle of 60°. As *Swift*-BAT is a local sample, we assume the R15 distribution locally and add the same redshift evolution as U14. The details of the update are explained in Appendix A. We found that this update still leaves the Compton-thick counts largely underestimated. Therefore, we used a neural network to modify the XLF further. In this section, we describe this neural network.

5.1. Neural Network to Optimize XLF

In order to reasonably modify the luminosity function to find a solution that fit all the observed constraints, we used a neural network. This neural network finds all the XLFs that fit the CXB given a set of input spectra. The spectral parameter distributions of these input spectra can be luminosity, redshift, and/or $N_{\rm H}$ dependent.

The distinct contribution to the CXB from each $N_{\rm H}$ bin is discussed in Section 2. However, different proportions of AGNs within the same absorption range, but with different luminosities, can produce the same CXB. To break the degeneracy within luminosity bins, all available number counts can be used for cross-validation.

Therefore, the neural network modifies the space densities to find all the solutions that fit the CXB. In this way, the X-ray background acts as a training set. The rest of the number counts and Compton-thick fractions act as a test set to verify the accuracy of the output models.

We carried out the changes as follows. We convert the U14 +R15 XLF described in Appendix A into a 3D matrix of space densities rather than a parametric function because it provides more flexibility to apply changes. This is a 3D matrix with dimensions z, L_{2-10}, and $N_{\rm H}$, and a simple linear interpolator will provide space densities at any (z, L_{2-10}, and $N_{\rm H}$) coordinate. It differs from the B15 final product, as there is no binning involved. B15 space densities are flat over the width of each 3D bin, whereas the space densities in our matrix vary continuously, similar to U14 and A15.

A neural network is used to tune this matrix so that it produces an increasingly better fit to the CXB. This neural network employs back-propagation and gradient descent algorithms, which are described in Appendix B.

We summarize our approach to deriving a new XLF in Figure 6. After optimizing the neural network for best performance, the best configuration was as follows: we divided the matrix reweighting into 15 blocks, i.e., three $N_{\rm H}$ bins (unabsorbed, Compton-thin, and Compton-thick) times five luminosity bins ($\log(L_{2-10}/\mathrm{erg\,s^{-1}})$: 41–42, 42–43, 43–44, 44–45, 45–47). The neural network has 15 input neurons, and each block is input into each neuron. The weights associated with each input neuron are the factors by which all space densities in each of these blocks are renormalized. After renormalization using these weights, CXB is calculated using the pre-defined spectra and this modified XLF. The neural network then calculates the cost function, which is the sum of squares of the difference between the observed CXB and the model prediction, divided by $2\times$ the number of observed data points. We use CXB observed data points from *Chandra* COSMOS (Cappelluti et al. 2017), *RXTE* (Revnivtsev et al. 2003), and *Swift*-BAT (Ajello et al. 2008), as these are the most updated estimates of the CXB. After calculating costs, the neural network then updates the space densities in these 15 bins simultaneously by calculating derivatives of the cost function with respect to the weights.

We initialize weights for the 15 neurons randomly between 0.3 and 5 and run 100 neural networks in parallel to find all the solutions that converge. Some parallel networks sometimes get trapped in local minima or diverge. We consider all branches that converge to costs $\leqslant$5.0, as it roughly corresponds to a reduced $\chi^2 \leqslant 2$ and should not be ruled out without cross-validation. We used the CXB as a training set and then cross-validated the resulting XLFs on the rest of the observed constraints: the number counts and the Compton-thick fractions. If an XLF fits the CXB with a reduced $\chi^2 < 2.0$, it has contributions from the three absorption bins (unabsorbed, Compton-thin, and Compton-thick) in correct proportions. However, different distributions in luminosity bins can produce the same CXB. The degeneracy in distribution in luminosity bins is broken by choosing the solution that minimizes reduced χ^2 with respect to all the observed number counts/Compton-thick fractions.

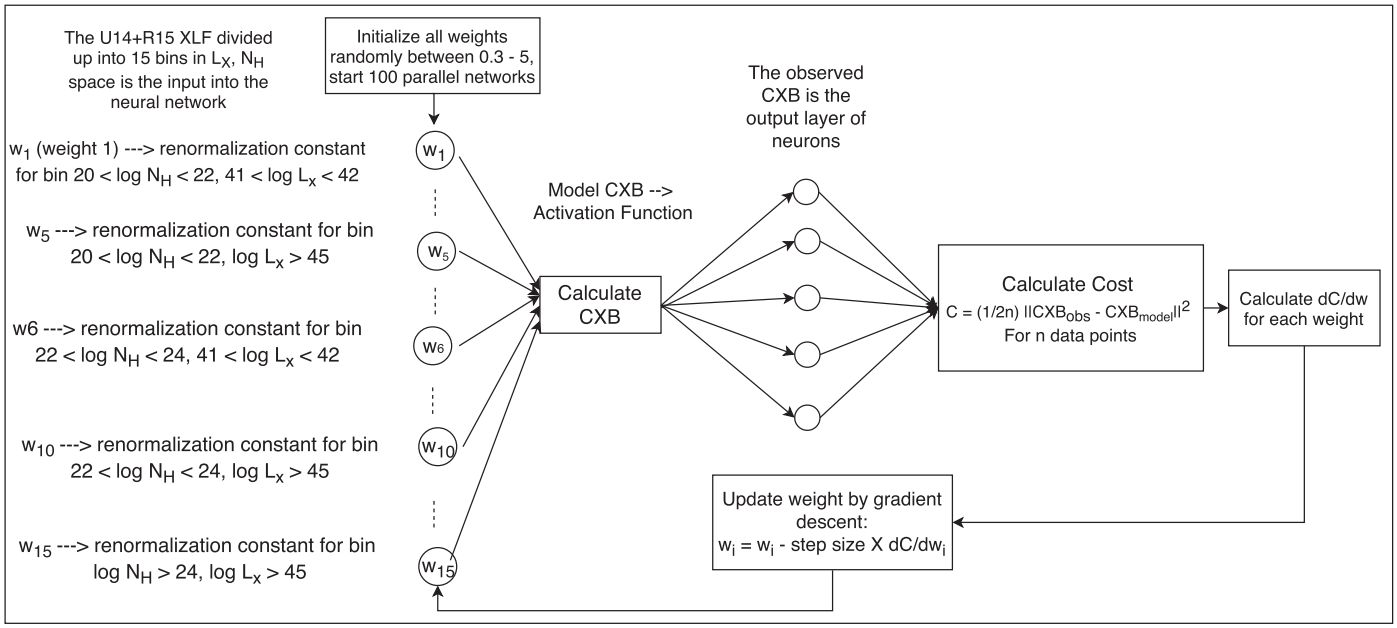

Figure 6. Summary of our neural network to find space densities that reproduce the X-ray background. The result is then validated using number counts and Compton-thick fractions from *Chandra*, *XMM*, *Swift*-BAT, and *NuSTAR* surveys.

Table 3
Summary of Approaches Taken to Formulate XLF in Recent Works[a]

MODEL	APPROACH	RESULTS
Ueda et al. (2014)	Maximum likelihood methods on survey data to formulate XLF and N_H distribution	Parametric function
Aird et al. (2015)	Bayesian analysis of survey data	Parametric function
Buchner et al. (2015)	Bayesian analysis of survey data	Nonparametric space density 3D grid
This work	Neural network fitting to X-ray background, cross-validation using number counts/fractions from surveys	Nonparametric space density 3D grid

Note.
[a] The details of the spectra for each model are given in Table 1, where this work uses observed parameter distributions from *Swift*-BAT, explained in Section 5.2.

The number of parallel networks is limited by computational power. Increasing the number of parallel networks increases the probability of a quick convergence, as the number of steps needed to reach a minimum via gradient descent is sensitive to initial position. However, each point in the CXB requires a numerical integration over redshift, L_X, N_H, and energy, using Monte Carlo sampling. Therefore, the number of multiple processes that can be run is limited.

We present a summary of the approaches taken to formulate U14, A15, B15, and this work in Table 3.

5.2. A Discussion on Spectral Parameters

To calculate the expected CXB and number counts from the XLF, we have to integrate the AGN spectra over a range of energies for all AGNs. Because of the uncertainty in spectral parameters due to various biases and parameter couplings, as explained in Section 2.1, we tested our neural network with different combinations of Γ, R, and E_{cutoff}. The combinations of spectral parameters used are determined by observed values that exist in the literature. A representative sample is listed in Table 4. The XSPEC syntax of the spectral model is FSCATT × CUTOFFPL + WABS × PEXMON + BNTORUS × HIGHECUT.

For all five sets of spectra, the scattered component is proportional to the initial cutoff power law, with a scattering fraction (f_{scatt}) of 0.01. The torus is modeled using BNTORUS. The value of the half-opening angle is drawn from a uniform distribution between 55° and 61° (Section 5.3.1 of Ricci et al. 2017). For unabsorbed sources, the physical inclination angle should be pole-on (Masini et al. 2016). BNTORUS assumes line-of-sight column density for all angles, so the change in observed spectra with respect to inclination angle is very small. However, to be physically consistent, we fix the inclination angle for $\log(N_H/\mathrm{cm}^{-2}) < 21$ objects at 25°, smaller than the opening angle of the torus. The inclination angles for $\log(N_H/\mathrm{cm}^{-2}) = 21$–24 objects are larger than the opening angle by 15°, and the inclination angle of $\log(N_H/\mathrm{cm}^{-2}) > 24$ is fixed at the maximum possible value of 87°. The reflection component is modeled using the self-consistent PEXMON model, with an inclination angle of 30° (all parameters typical of *Swift*-BAT AGNs).

Spectral Set 1 in Table 4 is the observed spectral parameter distributions from the *Swift*-BAT 70-month catalog. For the intrinsic cutoff power law, we draw Γ from two normal distributions: $\langle\Gamma\rangle \simeq 1.8$ and $\sigma_\Gamma = 0.24$ for unobscured AGNs, and $\langle\Gamma\rangle \simeq 1.72$ and $\sigma_\Gamma = 0.31$ for obscured AGNs. We choose cutoff energy values of the 161 objects for which this value was properly constrained and draw from that distribution to produce AGN spectra. The reflection scaling factor is drawn from two

Table 4
Spectral Parameters Used to Construct Spectra in This Work

Spectral Set	Photon Index $\langle\Gamma\rangle$	Refl. Scaling Factor (R)	$E_{\rm cutoff}$ (keV)	$f_{\rm scatt}$
1[a]	1.72 (obscur), 1.8 (unobsc)	0.37 (obscur), 0.83 (unobsc)	76	≃1%
2[b]	1.72 (obscur), 1.8 (unobsc)	0.37 (obscur), 0.83 (unobsc)	200 ± 29	≃1%
3[c]	1.8	0.83	200 ± 29	≃1%
4[d]	1.72 (obscur), 1.8 (unobsc)	0.37 (obscur), 0.83 (unobsc)	128 ± 46	≃1%
5[e]	1.96	0.37 (obscur), 0.83 (unobsc)	200 ± 29	≃1%

Notes.
[a] Observed parameters determined by detailed X-ray spectral fittings to *Swift*-BAT 70-month survey sources by Ricci et al. (2017).
[b] The cutoff energies measured in *Swift*-BAT can only be adequately constrained when the value is lower than 100 keV, so using a distribution that takes the lower limits into account using a Kaplan–Meier estimator, the true median is found to be 200 keV.
[c] Γ and R for unobscured sources from *Swift*-BAT, and $E_{\rm cutoff} = 200$ keV.
[d] Same parameter distribution as Spectrum 1, with $E_{\rm cutoff} = 128 \pm 46$ keV Gaussian distribution. This cutoff energy distribution is reported by Malizia et al. (2014).
[e] Spectrum 2 parameter distribution, with $\Gamma = 1.96 \pm 0.1$, the median $\Gamma_{\rm BAT}$ for non-blazar AGNs as observed in the *Swift*-BAT 70-month sample, consistent with Nandra & Pounds (1994), Gilli et al. (2007), and U14.

Gaussian distributions: ($\langle R\rangle = 0.83$, $\sigma_R = 0.14$) and ($\langle R\rangle = 0.37$, $\sigma_R = 0.11$) for unobscured and obscured AGNs, respectively. These $\langle R\rangle$ were calculated by Ricci et al. (2017) by taking the upper and lower limits in R into account to produce a representative median for obscured and unobscured sources. The lower $\langle R\rangle$ value for obscured sources could arise because the reflection component from the accretion disk is higher for objects that are observed pole-on than for the ones that are observed edge-on.

To account for the fact that the observed cutoff energies are biased against high values (i.e., $E > 100$ keV), we attempted Spectral Set 2, where the observed values of Γ and R are unchanged, and cutoff energy is drawn from a Gaussian distribution of $\langle E_{\rm cutoff}\rangle = 200$ keV and $E_{{\rm cutoff},\sigma} = 29$ keV, as found using the Kaplan−Meier estimator on observed values. For Spectral Set 3, we use $\langle\Gamma\rangle$ and $\langle R\rangle$ for unobscured *Swift*-BAT sources and a cutoff energy of 200 keV, as there is a possibility that the difference in spectral parameters between obscured and unobscured objects arise owing to imperfections in the modeling of the obscurer. For Spectral Set 4, we adopted a Gaussian cutoff energy distribution with $\langle E_{\rm cutoff}\rangle = 128$ keV and $E_{{\rm cutoff},\sigma} = 46$ keV, as reported in Malizia et al. (2014) keeping all other parameters identical to Spectral Set 1. In Spectral Set 5, we adopt $\langle E_{\rm cutoff}\rangle = 200$ keV and $E_\sigma = 29$ keV along with $\langle\Gamma\rangle = 1.96$, which is the median $\Gamma_{\rm BAT}$ reported in Ricci et al. (2017), and consistent with high Γ values assumed in earlier models and observed values in Nandra & Pounds (1994), Gilli et al. (2007), and U14. The five sets of spectra in each $N_{\rm H}$ bin are shown in Figure 7. The results for these spectral analysis are discussed in Section 6.

6. Results and Discussion

We find a modified XLF that satisfies all observed constraints assuming the observed *Swift*-BAT 70-month spectral parameter distributions (Spectral Set 1 in Table 4). The results for Spectral Sets 2, 3, and 4 are shown in Figure 8. For Spectral Set 2, where the observed values of Γ and R are unchanged but the cutoff energy is drawn from a Gaussian distribution of $\langle E_{\rm cutoff}\rangle = 200$ keV and $E_\sigma = 29$ keV, the CXB at $E > 30$ keV is generally overestimated. We demonstrate the cause of this overestimation in Figure 8. In the top left panel of the figure, the unabsorbed contribution to the CXB is fixed to perfectly reproduce observations at $E < 2$ keV. Generally, the Compton-thin contribution becomes more significant at $E > 2$ keV and contributes to reproducing the slope of the CXB between 3 and 10 keV. However, in the figure, this region of the CXB is underestimated, whereas the CXB at $E > 30$ keV is overestimated. The Compton-thick contribution to 3–10 keV is much smaller than at $E > 20$ keV, so increasing the Compton-thick contribution will improve fits at 3–10 keV minimally but increase overestimation at $E > 30$ keV.

Similarly, for Spectral Sets 3 and 4, either the CXB is overestimated at high energies ($E > 30$ keV) or the slope cannot be matched at lower energies ($E < 10$ keV). Although Spectral Set 4 provides much more improved fits to the CXB, the Compton-thick contribution is very low and does not match observed number counts.

We obtain the best fit to all constraints using Spectral Set 5, where we adopt $\langle E_{\rm cutoff}\rangle = 200$ keV and $E_\sigma = 29$ keV along with $\langle\Gamma\rangle = 1.96$. Our analysis indicates that to fit the CXB, the effective mean of Γ and $E_{\rm cutoff}$ distributions has to be such that if $\langle E_{\rm cutoff}\rangle < 100$ keV then $\langle\Gamma\rangle \simeq 1.7$–$1.8$, or if $\langle E_{\rm cutoff}\rangle \geqslant 200$ keV then $\langle\Gamma\rangle > 1.8$. This is possibly a consequence of the correlation between the two parameters. Since the cutoff energies and Γ values in *Swift*-BAT are constrained together, the results of the spectral fit for these two parameters are not independent. However, we do find a closer fit to the observed constraints using a higher Γ and the unbiased $\langle E_{\rm cutoff}\rangle$ value of 200 keV.

The final results of our analysis are shown in Figures 9–17, where we fit all the population synthesis models to observations. For clarity, we only show solutions for our best-fit results for Spectral Set 5 (solid purple line in all figures) and include the Spectral Set 1 results (dotted purple line) for comparison. Our final population synthesis model is composed of Spectral Set 5 and the XLF associated with it, which fits all the observed constraints listed in Table 2. Figure 9 shows that the XLF produced in this work has a shape similar to U14, monotonous and smooth, but with a somewhat wider bend than a double power law. At $\log(L_{2-10}/{\rm erg\ s^{-1}}) < 44$, the normalization is closer to the B15 constant slope prior median prediction. We plot our final result in the $\log(N_{\rm H}/{\rm cm^{-2}}) = 20$–$24$ range with U14. Figure 10 observed data points in the same absorption bins, at four different redshifts. Figure 9 shows that the U14 binned data points are reproduced by this work as well.

The top panels of Figure 10 show the absorption functions for U14, B15, and A15 integrated up to $z \sim 0.1$. The top panels show only the fraction of objects in each bin, normalized in the

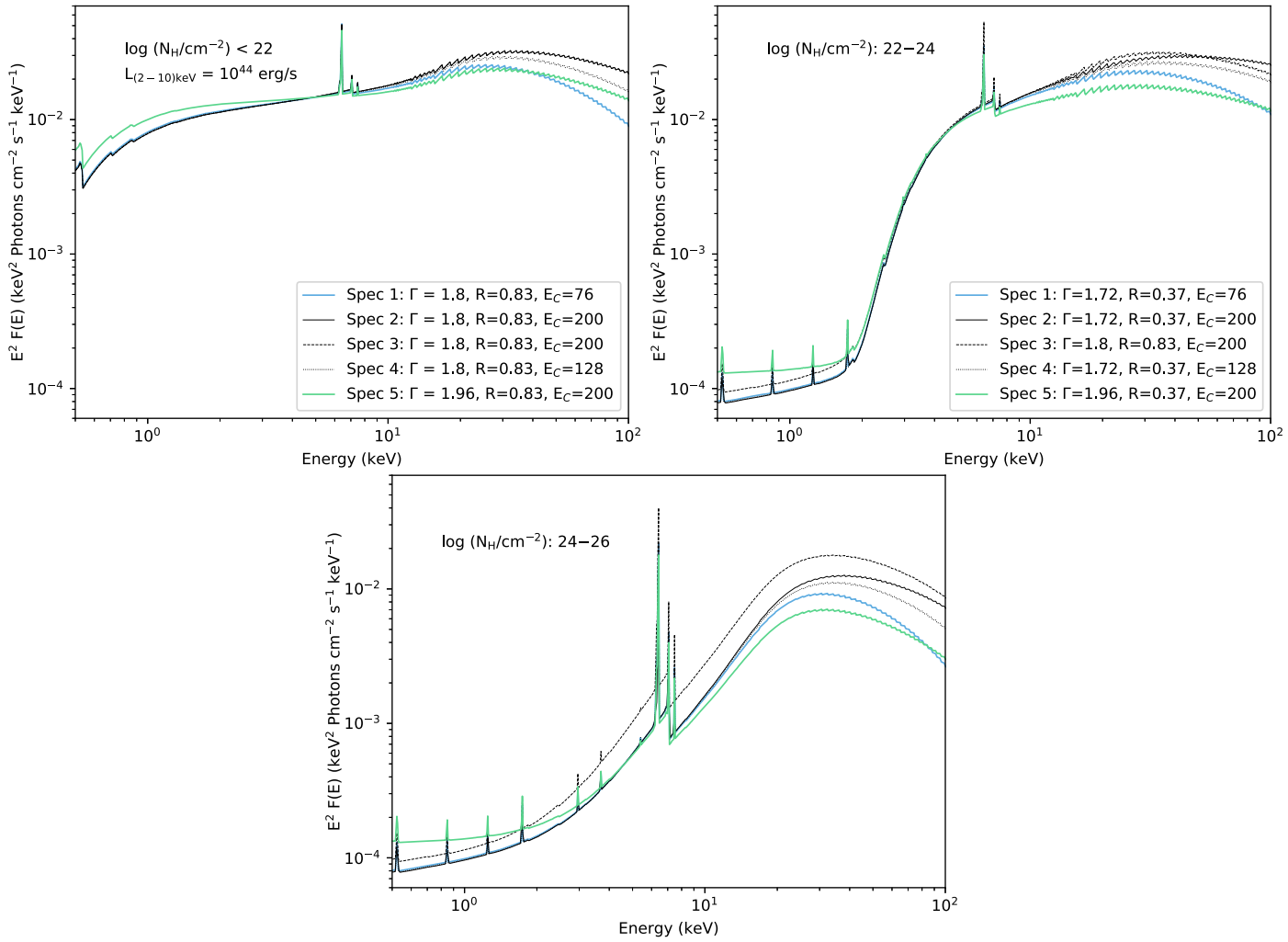

Figure 7. Resultant spectra from the five spectral parameter distributions explored in this work to find the XLF that fits all observed constraints. Top left: spectra of an unabsorbed object; top right: spectra of a Compton-thin object; bottom: spectra of a Compton-thick object. The same parameters are used for both Compton-thin and Compton-thick objects. All the spectra have an intrinsic X-ray 2−10 keV luminosity of 10^{44} erg s^{-1}. The values of the parameters come from the *Swift*-BAT 70-month survey (Ricci et al. 2017) and other spectral fittings (Nandra & Pounds 1994; Malizia et al. 2014; Ueda et al. 2014).

$\log(N_{\rm H}/{\rm cm}^{-2}) = 20$–24 region, while the bottom panels show the absolute number of objects per deg^2. The obscuration-bias-corrected absorption function for the *Swift*-BAT 70-month catalog, calculated by R15, is also plotted in the top panels, for both of the assumed torus opening angles. The low- and high-luminosity bins are in the left and right panels, respectively. This work is in agreement with the $N_{\rm H}$ distribution derived by R15 at $\log(N_{\rm H}/{\rm cm}^{-2}) < 24$ but predicts much higher fractions of Compton-thick objects, similar to B15. This figure sheds light on the discrepancy between this work and some of the previous works. The space densities of unabsorbed and Compton-thin objects in this work are comparable to those of previous works, but the number densities of Compton-thick objects are much higher than in U14 and A15 in both bins, and equal to B15 in the lower-luminosity bin and higher in the higher-luminosity bin, as shown in the bottom panels of Figure 10.

We take the A15 galaxy contribution to the CXB into account to avoid overestimating AGN space densities. The A15 galaxy contribution is calculated using a simple power law, with $\Gamma = 1.9 \pm 0.2$, that results in a constant (with respect to energy) contribution of $\simeq$1.7 keV^2 cm^{-2} s^{-1} keV^{-1} sr^{-1} to the CXB at $E < 100$ keV. Observations show that starburst galaxy spectra drop off very quickly above 10 keV (Wik et al. 2014; Lehmer et al. 2015; Yukita et al. 2016), and a cutoff power law is more appropriate. Therefore, we introduce a uniform distribution of cutoff energies between 20 and 30 keV to the spectra (Persic & Rephaeli 2002, 2003; Treister et al. 2010; Wik et al. 2014; Lehmer et al. 2015; Yukita et al. 2016) and recalculate the contribution from galaxies using the A15 galaxy luminosity function. The resulting galaxy X-ray background drops off rapidly at $E > 7$ keV. We add this contribution to the CXB predictions from all models.

6.1. CXB

Figure 11 and Table 5 summarize the fits to the CXB by prior XLFs and this work. The CXB is an important assessment of X-ray population synthesis models: individual surveys and number counts from these surveys can be affected by cosmic variance, but data for the CXB come from a number of different experiments, in general averaged over very large areas, and converge on a similar shape (we show the latest data in the plot for better presentation).

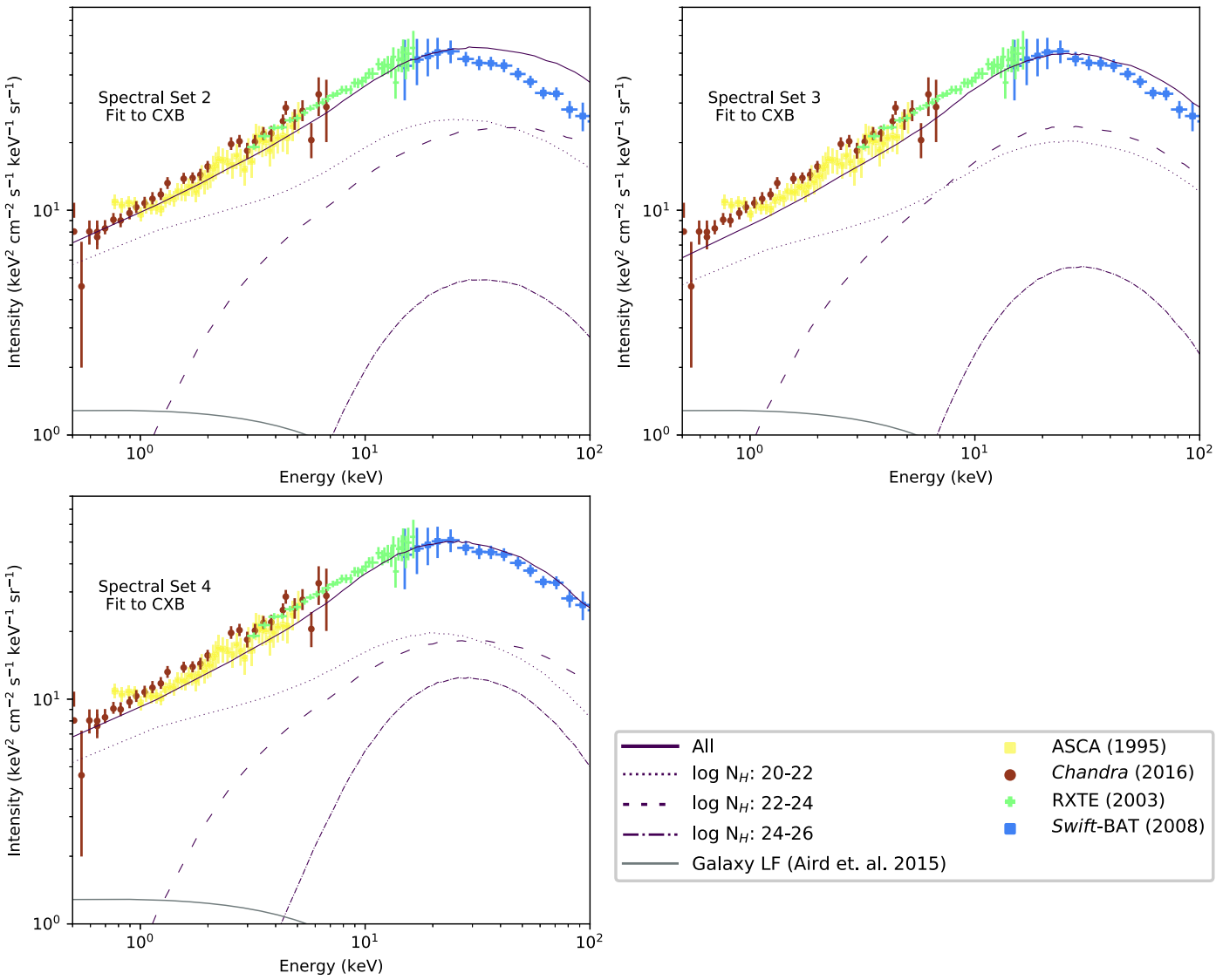

Figure 8. CXB data points fitted with three different assumed AGN spectra. Top left panel: the assumed spectra are from Spectral Set 2 from Table 4. Unabsorbed AGNs (dotted line) dominate the $E < 1$ keV region, so we fix the unabsorbed fraction such that this region is well fitted. Changing the unabsorbed contribution will over- or underproduce the CXB in this region. The Compton-thin objects (dashed line) contribute heavily in the 3–10 keV region, where the CXB is underestimated by $\geqslant 3\sigma$ with respect to *RXTE* data. Increasing the Compton-thin contribution will improve the fit in this region but overestimate the CXB at >30 keV, even with a negligible contribution from Compton-thick objects (dotted-dashed line). Increasing the Compton-thick fraction will contribute minimally in the 3−10 keV region but will lead to greater overestimation at higher energies, as the Compton-thick contribution peaks at 20–60 keV. The black solid lines in all three panels show the galaxy contribution to the CXB, calculated using the A15 galaxy LF. Top right panel: Spectral Set 3 adopts a higher photon index (1.8) and reflection coefficient (0.87) for absorbed objects, equal to those of unabsorbed objects. This model reaches better agreement with the CXB than Spectral Set 2 at $E > 30$ keV but continues to overestimate it, and it does not match all observed constraints. Bottom left panel: Spectral Set 4 adopts the same reflection parameter and photon index distributions as Spectral Set 2, but a lower cutoff energy of 128 ± 46 keV. It produces improved (but not perfect) fits to the CXB compared to Spectral Sets 2 and 3 but heavily underestimates Compton-thick number counts and fractions, as a higher Compton-thick contribution will overproduce the CXB at $E > 30$ keV.

The CXB plotted in Figure 11 for each model is our computation using the prescriptions in each work, and not taken directly from the results plotted in those papers. The discrepancy in the CXB model predictions of U14 and A15 models between this plot and those published in the corresponding papers is addressed in Appendix C. We find a better fit to the CXB than previous XLFs, as shown Figure 11 and Table 5. Of the previous XLFs, U14 produces the best match to the CXB. Originally, B15 did not assume any cutoff energy, which leads to overproduction of the CXB at high energies. We found that a cutoff energy of 200 keV greatly improves B15 fits, especially for the median constant slope prior. For B15, the range spanned between constant value prior and constant slope prior results illustrates the variety of CXB predictions possible from fitting XLFs with no shape imposed. The constant slope prior fits the CXB results more closely, so we ignore the constant value prior results in the remaining analysis.

6.2. Overall Number Counts

Figure 9 shows that the XLF presented in this work roughly follows a bending power-law shape similar to U14—which is expected, as U14+R15 is the basis of our function. We fit overall counts from *XMM*, *Chandra*, *Swift*-BAT, and *NuSTAR* using these XLFs to verify that our population synthesis model reproduces these observations.

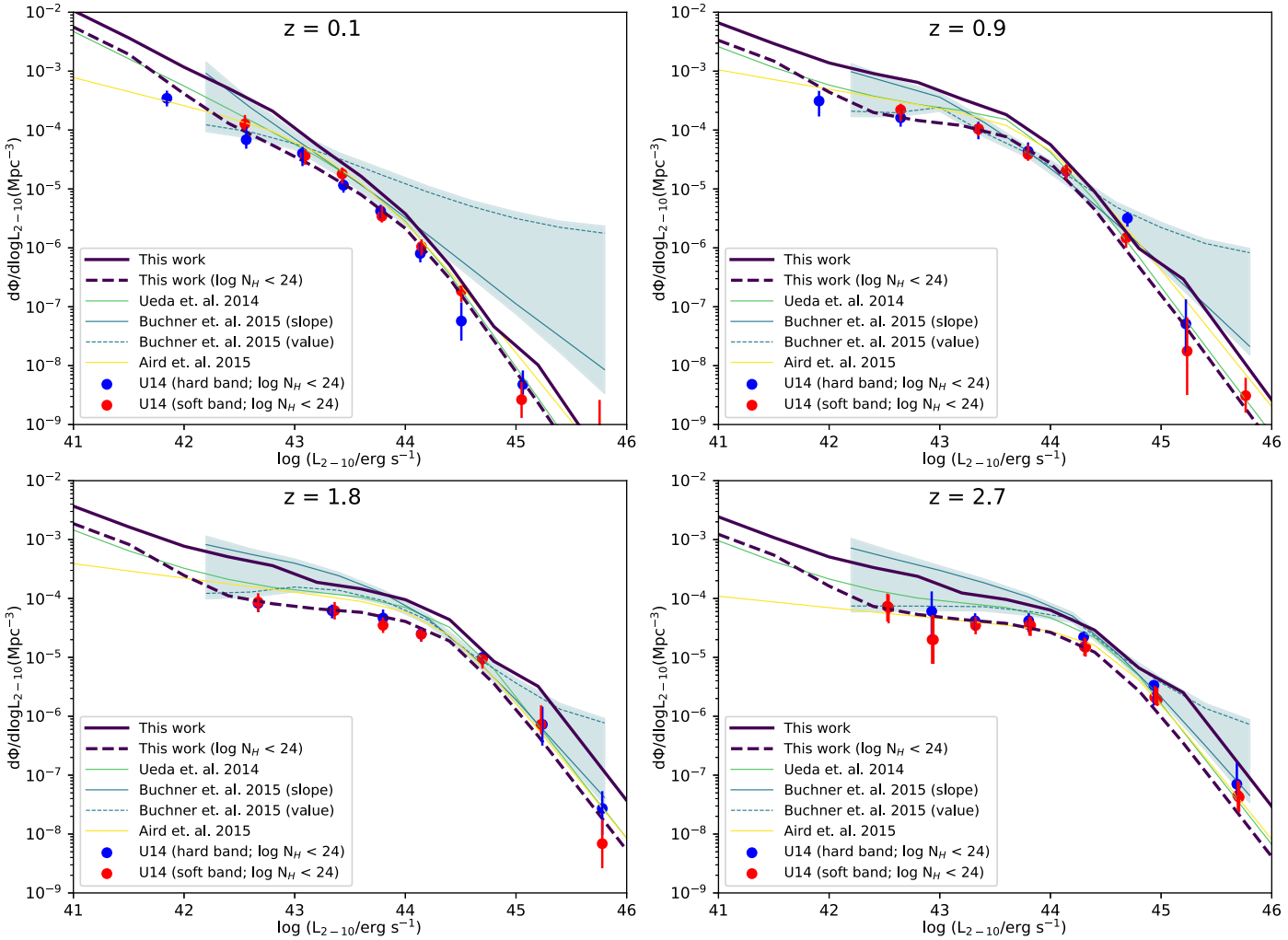

Figure 9. Number of objects per comoving Mpc^3 against log L_x for $z = 0.1$ (top left), $z = 0.9$ (top right), $z = 1.8$ (bottom left), and $z = 2.7$ (bottom right), summed over all absorption bins, including Compton-thick objects (solid lines), and summed in the log $N_H = 20$–24 bins (dashed lines). The models are this work (purple lines), U14 (light-green line), A15 (yellow lines), B15 median of constant slope prior (gray solid lines), and median of constant value prior (gray dashed lines). The shaded gray region is B15 uncertainty (1st–99th percentile). The blue and red data points are binned counts in the log $N_H = 20$–24 range from Ueda et al. (2014), in the hard- and soft-X-ray-selected bands, respectively. The overall XLF in the log $N_H = 20$–24 for this work (dashed purple line) is also given for comparison with data points.

The XLF formulated using our neural network reproduces the CDFS number counts in both soft and hard bands down to the faintest fluxes, as shown in Figure 12. The figure contains all of the soft-band (0.5−2 keV) and hard-band (2–7 keV) number counts for *XMM-Newton* and *Chandra* surveys. U14 and A15 fit these number counts down to flux levels of $10^{-15.5}$ erg cm^{-2} s^{-1}, but at fainter levels they start to underestimate counts by several σ. B15 overestimates counts in the 0.5–2 keV band at flux limits fainter than $10^{-14.5}$ erg cm^{-2} s^{-1} but fits the 2−7 keV band well. As there are many data sets plotted on these two plots, we made interactive versions of these plots available in the online Journal.[12] The older 4 Ms counts of CDFS (Lehmer et al. 2012) are also included in that plot.

The *NuSTAR* observed overall counts in the 8–24 keV band (Harrison et al. 2016) are shown in Figure 13. They are fitted well by this work, B15, and U14. A15 overestimates the counts in the lower fluxes.

We calculated *Swift*-BAT number counts using Ricci et al. (2017) data in the 14–195 keV region, as shown in Figure 14. This work provides the best fit to these number counts. U14 slightly overestimates these counts by 1σ–2σ. A15 overestimates the counts by 2σ–4σ at all fluxes, whereas B15 underestimates these counts by 1σ–4σ, with the discrepancy increasing at lower fluxes.

6.3. Compton-thick Number Counts and Fractions

The *Chandra* COSMOS-Legacy Compton-thick counts span the highest redshift space and are a result of the Bayesian analysis presented in Lanzuisi et al. (2018) that considers the total probability of being Compton-thick for each object in their sample. They use this probability (fraction) to calculate number counts. The model fits to these data are shown in Figure 15. Our models, both Spectral Set 1 and 5, fit these data better than prior XLFs. B15 also produces a close fit. U14 underestimates the counts, as does A15.

Lansbury et al. (2017) calculated *NuSTAR* Compton-thick number counts with low-redshift bias and an upper limit on

[12] See also https://yale.box.com/s/dzrn0zfjvi0eepc6w924yaixwgelt59m.

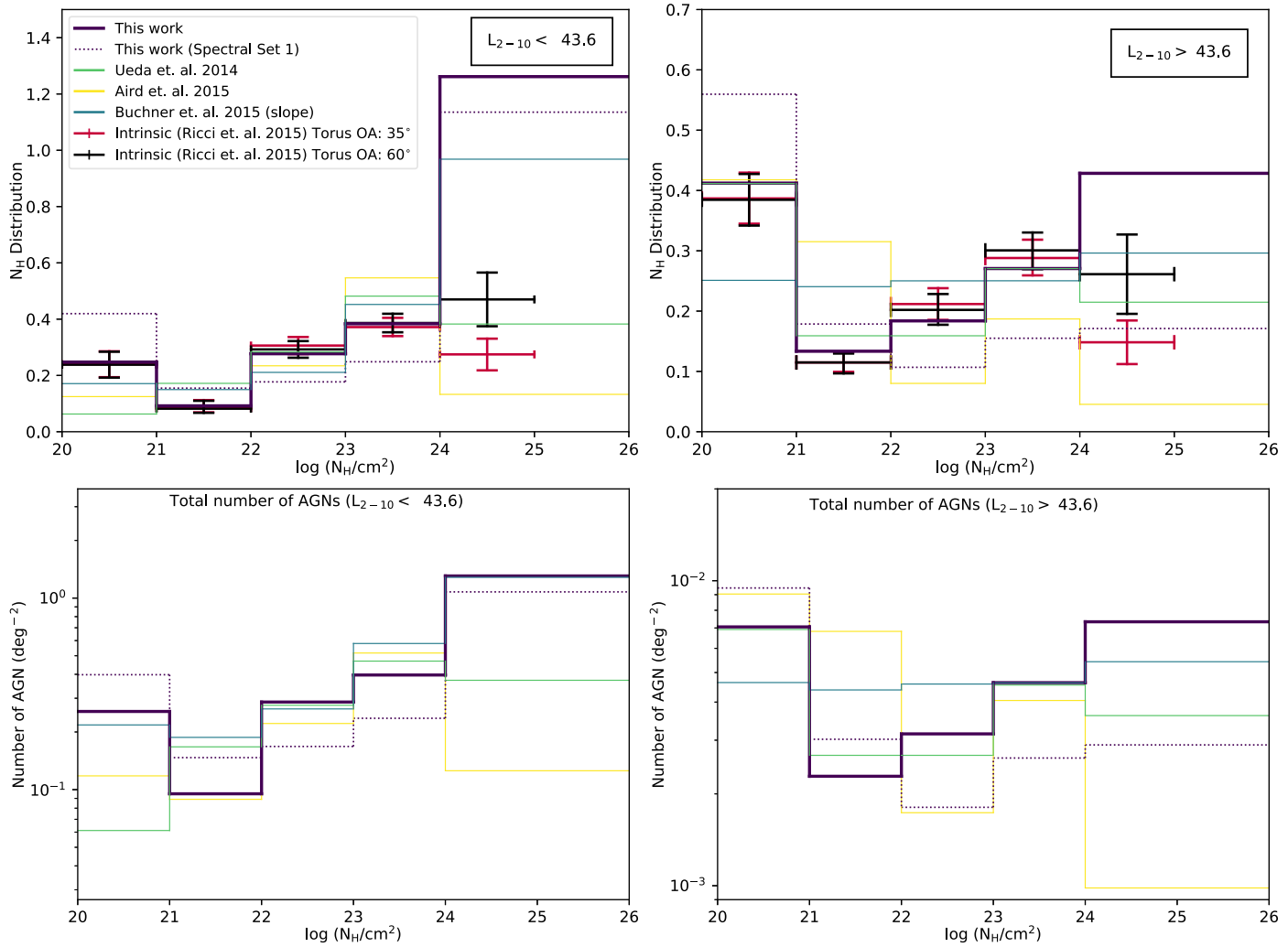

Figure 10. $N_{\rm H}$ distributions assumed for the present work and for previous population synthesis models. Top panels: $N_{\rm H}$ distributions for various models, integrated up to $z \simeq 0.1$ (solid lines), including the completeness-corrected (Ricci et al. 2015) distributions assuming two different geometries for the torus: an opening angle of 60° (black plus sign) and an opening angle of 35° (red plus sign). The observations are in the $\log(N_{\rm H}/{\rm cm}^{-2}) = 20$–25 range. The models are this work (purple line), Spectral Set 1 (dotted purple line, also from this work), U14 (light-green line), A15 (yellow line), and B15 (median of constant slope prior; gray solid line). All models assume that the number densities of objects in the $\log(N_{\rm H}/{\rm cm}^{-2}) = 24$–25 bin are equal to those of the $\log(N_{\rm H}/{\rm cm}^{-2}) = 25$–26 bin for all redshifts and luminosities, as there are very few data to constrain the $\log(N_{\rm H}/{\rm cm}^{-2}) = 25$–26 bin. Therefore, the model predictions are constant over these two absorption bins. Left panel: $N_{\rm H}$ distributions for the lower-luminosity bin ($\log [L_{2-10}/{\rm erg\ s}^{-1}] < 43.6$); right panel: those for the higher-luminosity bin ($\log [L_{2-10}/{\rm erg\ s}^{-1}] < 43.6$). Both panels are normalized in the $\log (N_{\rm H}/{\rm cm}^{-2}) = 20$–24 range. Bottom panels: total predicted number counts per square degree at each $N_{\rm H}$ bin, integrated to redshift = 0.1 in each luminosity bin.

Compton-thick counts without the bias, using four objects with extremely hard X-ray spectra from the *NuSTAR* Serendipitous Survey data. These counts are shown in Figure 16. Our model fit lies 2σ below the counts with low-redshift bias. B15 comes slightly closer to these Compton-thick number counts, and U14 underestimates these counts by $2\sigma-3\sigma$. The A15 Compton-thick counts are much lower than the observations. As explained in Lansbury et al. (2017), the sample is biased because the three lowest-redshift, highest-flux objects show evidence of being weakly associated with *Swift*-BAT AGN targets of *NuSTAR* observations, which have a higher tendency of galaxy clustering. The bias may be the cause of the discrepancy between the models and these number counts. The unbiased upper limit is calculated using only the highest-redshift object, which is consistent with prior XLFs and our results.

The Compton-thick fraction for the Lansbury et al. (2017) *NuSTAR* sample is shown in the left panel of Figure 17, along with the *Swift*-BAT observed 70-month and 3 yr Compton-thick fractions (these fractions were calculated in the 8–24 keV band by Lansbury et al. 2017). Our model fits all the fractions within 1σ–1.5σ; B15 fits the *NuSTAR* fractions properly but overestimates the *Swift*-BAT fractions by 2σ. U14 underestimates the *NuSTAR* Compton-thick fraction by 2σ but fits the *Swift*-BAT 3 yr survey fraction at high fluxes well. In the right panel of Figure 17, we show that our model's predicted Compton-thick fraction of 18% is higher than the *NuSTAR* UDS (Masini et al. 2018) observed Compton-thick fraction of 11.5%, but fits the *NuSTAR* COSMOS Compton-thick fraction (Civano et al. 2015) well. B15 fits the *NuSTAR* COSMOS Compton-thick fraction well but slightly overestimates the UDS fraction, while both U14 and A15 underestimate these fractions.

U14 is within 2σ of most of these counts and does fit the *Swift*-BAT Compton-thick fractions in Figure 17. A15 has much smaller Compton-thick number counts and fractions than the observed *NuSTAR* and *Swift*-BAT values. The reason

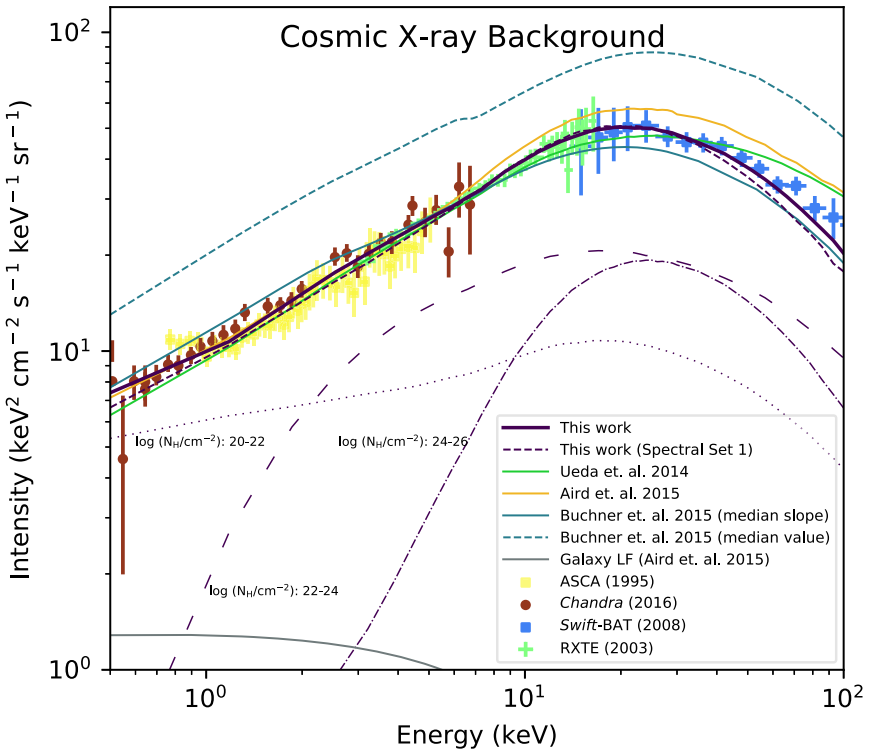

Figure 11. Empirical X-ray background (CXB) from *Chandra* COSMOS (red circles), *ASCA* (yellow squares), *RXTE* (green crosses), and *Swift*-BAT (blue squares). One outlying data point from *Chandra* COSMOS at 1.5 keV was removed owing to incorrect background subtraction. Models are this work (solid purple line), Spectral Set 1 results (dotted purple line, also from this work), U14 (light-green line), A15 (yellow line), B15 median of constant slope prior (gray solid line), and B15 median of constant value prior (gray dashed line). We added a cutoff energy of 200 keV to the B15 spectral model to bring the XLF in better agreement with the CXB at higher energies. A galaxy contribution has been added to each CXB model prediction, according to the A15 galaxy luminosity function (black solid line). Total contributions to the CXB from three absorption bins for this work are also shown: log (N_H/cm^{-2}) = 20–22 is shown by the dotted purple line, log (N_H/cm^{-2}) = 22–24 is shown by the sparsely dashed purple line, and log (N_H/cm^{-2}) = 24–26 is shown by the dotted-dashed purple line. The discrepancy in the CXB model predictions of U14 and A15 models between this plot and those published in the corresponding papers is addressed in Appendix C.

Table 5
Statistical Significance of the Match to X-Ray Background

CXB Constraint	Number of Data Points	This Work (χ^2) **Spec5** Spec1	Ueda et al. (2014) (χ^2)	Aird et al. (2015) (χ^2)	Buchner et al. (2015) (χ^2)[a] No E_C	E_C = 200 keV
Chandra COSMOS	25	**21.75** 58.3	70.84	17.36	68.43	55.91
RXTE	34	**17.98** 45.74	46.5	152.95	203.06	76.21
Swift-BAT	15	**11.66** 46.02	36.5	137.88	1099	69.79
Total	74	**51.4** 150.05	153.84	308.2	1370	201.9
Reduced χ^2		**0.87** 2.54	2.08	4.16	18.52	2.73

Note. Boldface shows results for the best-fit solutions.
[a] For B15, results for only the median constant slope prior are shown here.

behind this discrepancy is shown in the bottom panels of Figure 10—A15 has lower Compton-thick space densities compared to other models in both luminosity bins. This discrepancy might be caused by the statistical approach A15 used to derive the absorption function. Instead of calculating N_H of individual sources through X-ray spectral fittings as done by U14 and B15, they compare the 0.5−2 keV selected sample with the 2–7 keV sample, taking into account the shift in AGN spectra with redshift. A15 discusses the limitation in this approach in distinguishing Compton-thick sources from heavily absorbed Compton-thin sources. These uncertainties may have contributed to underestimation of Compton-thick number density.

The Compton-thick fractions found in this work and in B15, as shown in Figure 10, are much higher than in U14 and A15; this work fits the R15 fractions at log (N_H/cm^{-2}) < 24 (as shown in the figure), but the Compton-thick fraction is much higher than that derived by R15. This plot demonstrates why the U14+R15 update failed to reproduce the Compton-thick number counts. Our new model fits the *NuSTAR* and *Chandra* COSMOS-Legacy Compton-thick number counts significantly better because the Compton-thick number counts need to be higher than R15 corrections in both luminosity bins. U14, Ricci et al. (2015), and M. Balokovic (2019, in preparation) found that even *Swift*-BAT is not completely unbiased toward Compton-thick sources beyond log (N_H/cm^{-2}) ∼ 23, which

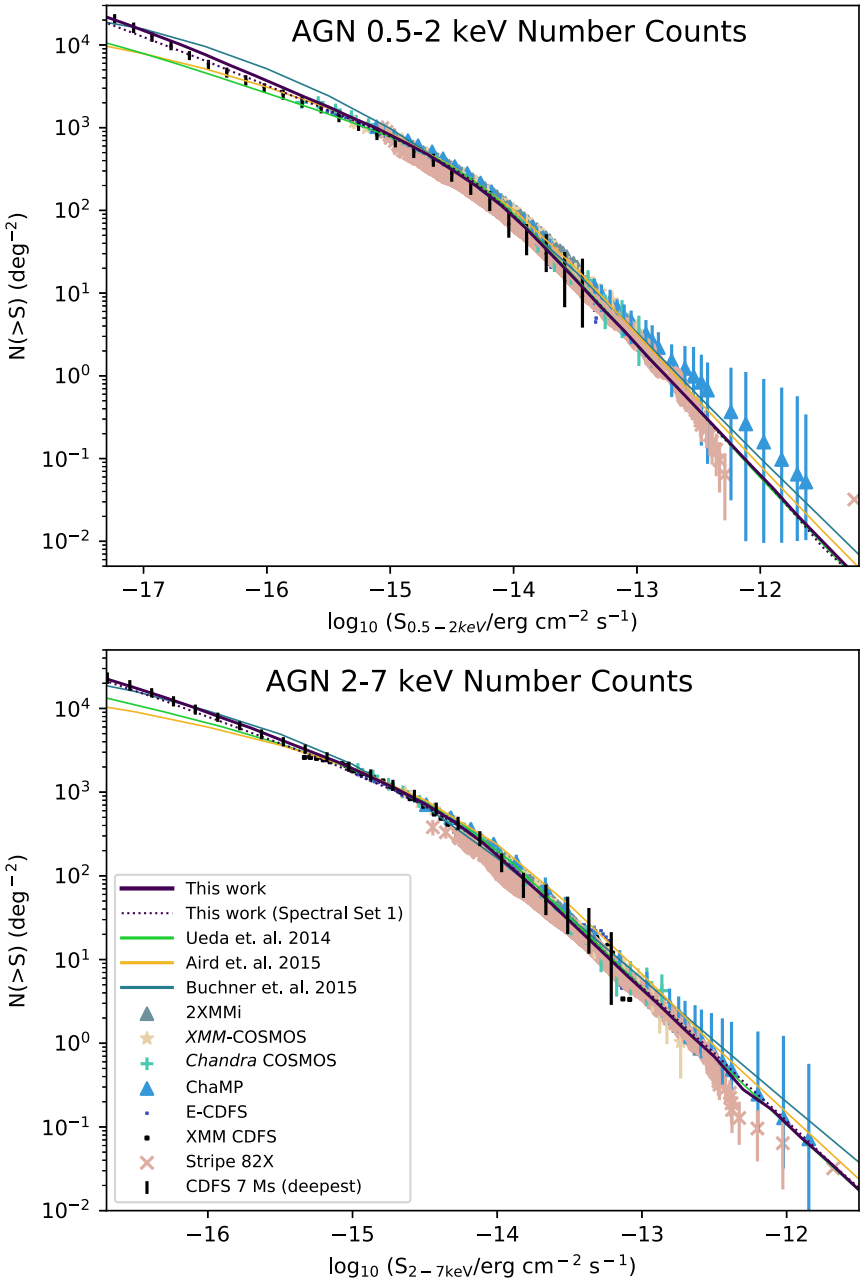

Figure 12. Number counts per square degree of the sky vs. X-ray flux, as observed in the *Chandra* 7 Ms (black circle + vertical error bars), 2*XMM*i (gray triangle), *XMM*-COSMOS (light-pink stars), *Chandra* COSMOS (green plus signs), ChaMP (blue triangles), Stripe 82X (pink crosses), E-CDFS (deep-blue dotted line), and *XMM*-CDFS (black dotted line) surveys (all references in text). The models are this work (Spectral Set 5, solid purple line), U14 (light-green line), A15 (yellow line), and B15 median of constant slope prior (gray solid line). Spectral Set 1 results are also shown by the dotted purple line. As all the data points cannot be seen in this static plot, an interactive version of this figure is available in the online Journal. Top panel: 0.5–2 keV number counts. Bottom panel: 2–7 keV band number counts. For the *Chandra* 7 and 4 Ms number counts in both bands, nearly all existing luminosity functions considered in this work underestimate the number counts, although the high flux number counts are generally well reproduced. The B15 constant slope prior median value reproduces the hard-band count for *Chandra* 7 Ms very well but overestimates the soft counts by $>2\sigma$ at log $(S_{0.5-2\ \mathrm{keV}}/\mathrm{erg\ cm^{-2}\ s^{-1}}) \simeq -16$.

could be the cause of the discrepancy between our model and the fractions derived by R15.

7. Conclusions

The most noteworthy aspect of our best-fit luminosity function is the high intrinsic Compton-thick fraction predicted by this model. Of the overall AGN population integrated up to $z \simeq 0.1$ (1.0), $50\% \pm 9\%$ ($56\% \pm 7\%$) is predicted to be Compton-thick by this model. This intrinsic Compton-thick fraction is consistent with observed number counts and fractions when flux, redshift limits, and bandwidths in different surveys are taken into account, as shown in Section 6.

This work generally has higher space densities of Compton-thick objects compared to the three prior XLFs, as shown in Figure 10. In the bottom panels of that figure, there is a comparison between integrated space densities from the local universe, up to $z = 0.1$, in two luminosity bins. In the low-luminosity bin, B15 has $\simeq$2% lower, U14 has $\simeq$72% lower, and A15 has $\simeq$91% lower Compton-thick space densities than

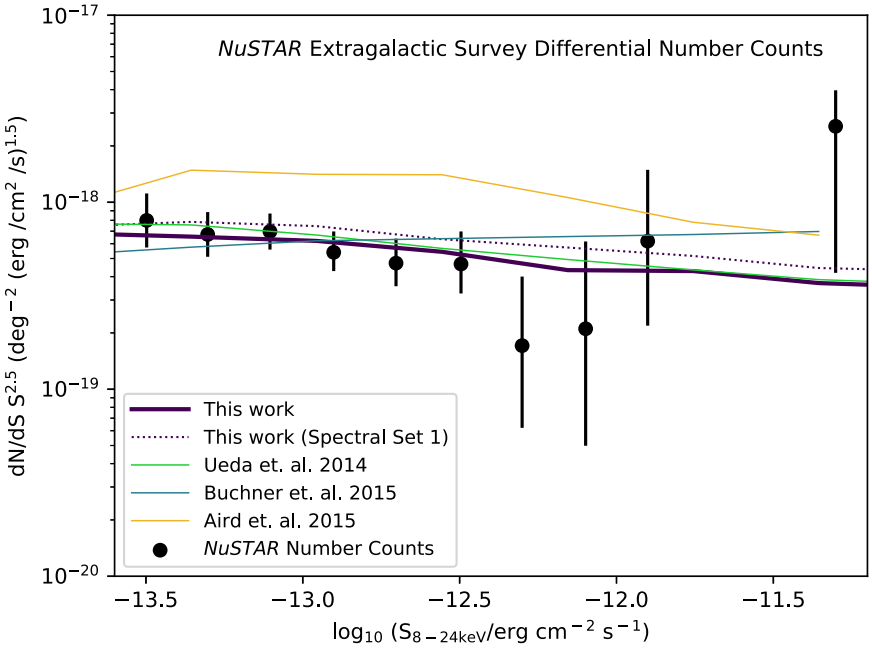

Figure 13. *NuSTAR* Extragalactic Survey number counts for AGNs. Black data points are the differential number counts calculated using the *NuSTAR* COSMOS, *NuSTAR* E-CDFS, *NuSTAR* EGS, and *NuSTAR* Serendipitous Surveys (Harrison et al. 2016). The models are this work (Spectral Set 5, solid purple line), U14 (light-green line), A15 (yellow line), and the B15 median of constant slope prior (gray solid line). Spectral Set 1 results are also shown by the dotted purple line.

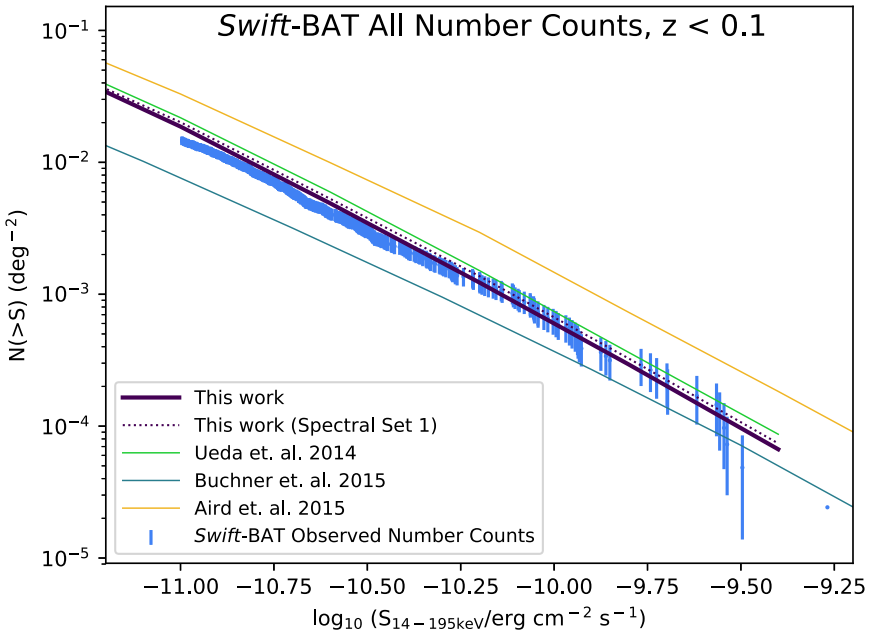

Figure 14. *Swift*-BAT overall number counts (blue circles with vertical error bars) calculated using the 70-month survey data (Ricci et al. 2017). The models are this work (Spectral Set 5, solid purple line), U14 (light-green line), A15 (yellow line), and the B15 median of constant slope prior (gray solid line). Spectral Set 1 results are also shown by the dotted purple line.

this work. In the high-luminosity bin, this work predicts the highest space densities: B15 has 26% lower, U14 has ≃51% lower, and A15 has ≃87% lower space densities of Compton-thick objects than this work.

The three nearest AGNs (≃4 Mpc), Circinus, NGC 4945, and Centaurus A, are all heavily obscured, which can be either due to a Compton-thick bias in the local universe or representative of the true AGN population. Obscured sources tend to be bright in IR owing to reprocessed emission. Matt et al. (2000) explored the IR and X-ray emission from some of the closest heavily obscured AGNs and found that the IR LF is 20 times the XLF in the local universe. Gandhi & Fabian (2003) also predict an obscured-to-unobscured ratio of 5:1 by formulating a population synthesis model where obscured AGNs are assumed to follow the same distribution as luminous IR galaxies. Fiore et al. (2008) selected sources with a very high mid-IR-to-optical ratio in the CDFS field and found that 80% ± 15% of these objects have no direct X-ray

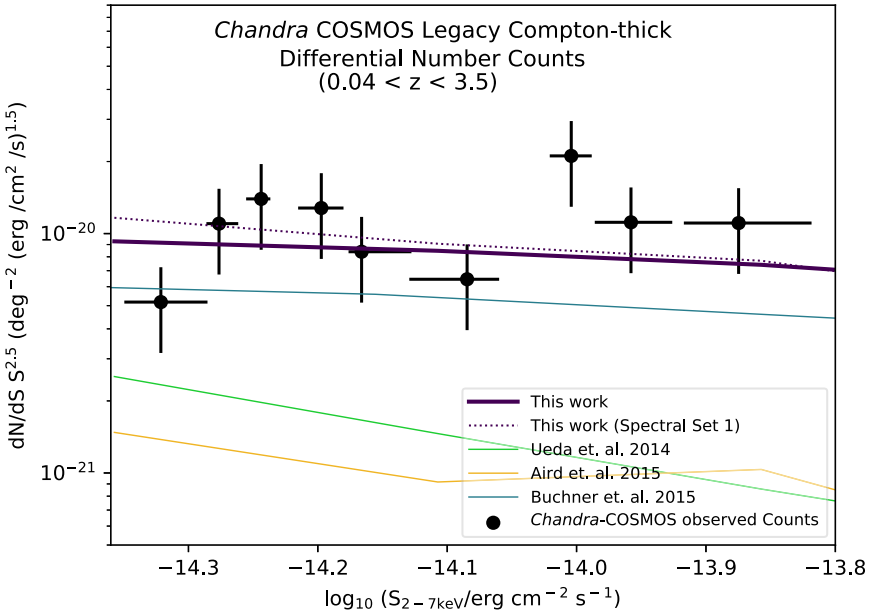

Figure 15. *Chandra* COSMOS-Legacy Compton-thick number counts. The data points are represented by black circles. The models are this work (Spectral Set 5, solid purple line), U14 (light-green line), A15 (yellow line), and the B15 median of constant slope prior (gray solid line). Spectral Set 1 results are also shown by the dotted purple line. The counts were calculated using 41.9 objects after a careful Bayesian analysis of the spectra of each object by Lanzuisi et al. (2018). The flux area curves for three different redshift ranges were calculated specifically using the spectra of Compton-thick objects. We use the appropriate areas by redshift and the fractional probability of each object of being Compton-thick to calculate number counts for the whole sample.

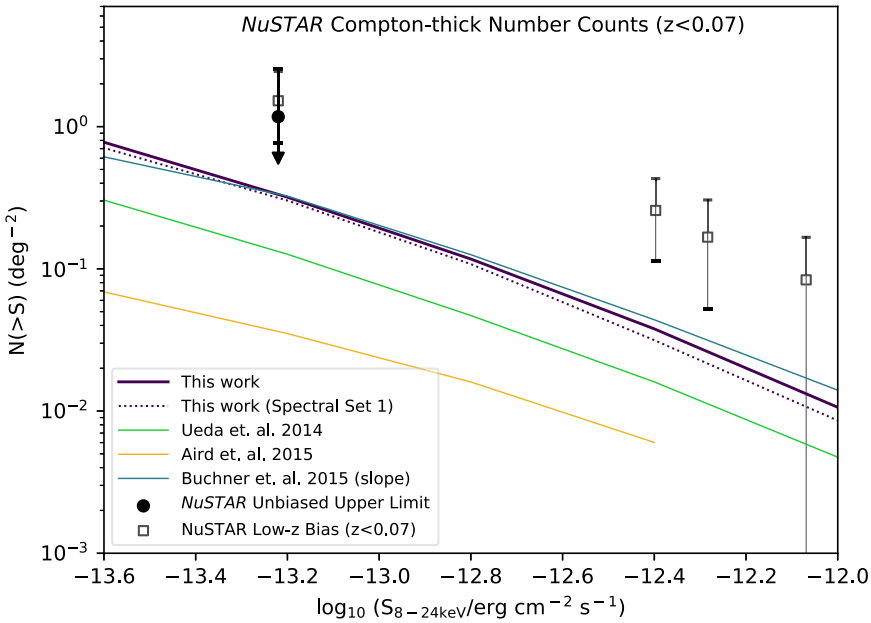

Figure 16. Compton-thick number counts in the 8–24 keV band from the *NuSTAR* 40-month Serendipitous Survey, calculated by Lansbury et al. (2017). The filled black circle is the unbiased upper limit on Compton-thick fraction for $z < 0.5$, and the gray number counts, calculated using four objects with extremely hard spectra, show the number counts with a low-redshift bias ($z < 0.07$). The models are this work (Spectral Set 5, solid purple line), U14 (light-green line), A15 (yellow line), and the B15 median of constant slope prior (gray solid line). Spectral Set 1 results are also shown by the dotted purple line. We find that the counts with the low-redshift bias are underestimated by all the luminosity functions, but this work and B15 are within 1.5σ, and U14 is within 2σ. All the XLFs are consistent with the unbiased upper limit.

detection in the hard X-ray band and are likely to be Compton-thick. Chen et al. (2015) show that the obscured fraction is 30%–70% in objects with high far-IR luminosities (4×10^{12} $L_{\rm sol}$); however, it is not clear what fraction of these obscured objects are Compton-thick. Ultraluminous IR galaxies, which tend to be gas-rich mergers (Clements et al. 1996), have Compton-thick fractions as high as 65% (Ricci et al. 2017), much higher than the *Swift*-BAT selected sample.

B15 and this work are closer to the high Compton-thick number counts and fractions observed by *Chandra*, *NuSTAR*, and *Swift*-BAT surveys. Previous works have stated that the most efficient way to find Compton-thick objects is using high-energy X-ray surveys ($E > 10$ keV; Gilli et al. 2007; Treister et al. 2009; Ballantyne et al. 2011), and the results of these surveys, particularly *NuSTAR* surveys, indicate higher Compton-thick space densities than those predicted by prior models. It has been

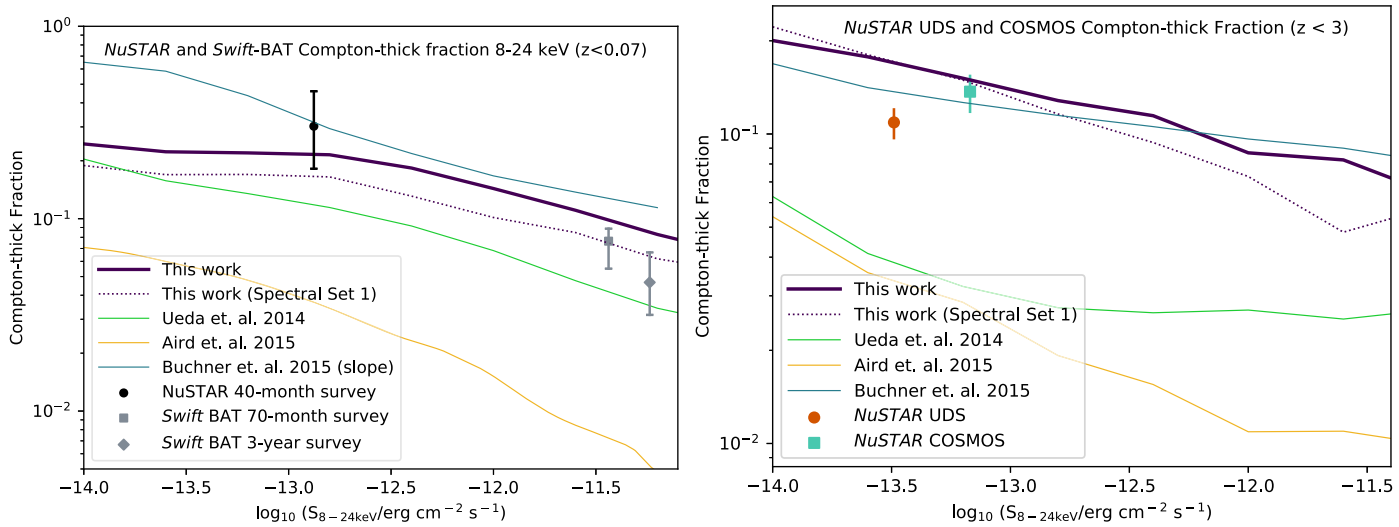

Figure 17. For both panels, the models are this work (Spectral Set 5, solid purple line), U14 (light-green line), A15 (yellow line), and the B15 median of constant slope prior (gray solid line). Spectral Set 1 results are also shown by the dotted purple line. Left: Compton-thick fraction in the 8–24 keV band from the *NuSTAR* 40-month Serendipitous Survey and the *Swift*-BAT 70-month and 3 yr surveys. B15 fits the *NuSTAR* Compton-thick fraction well but overestimates the *Swift*-BAT fractions. Spectrum 5 is within 1σ of the *NuSTAR* data and also fits the *Swift*-BAT data well. Spectrum 1 and U14 are 1σ below *NuSTAR* Compton-thick fraction but fit the *Swift*-BAT data well. Right: Compton-thick fraction in the 8–24 keV band from the *NuSTAR* UDS (Masini et al. 2018) and COSMOS surveys (Civano et al. 2015). These results span a higher redshift range ($0 < z < 3$) and are therefore plotted separately for clarity.

suggested that a smaller Compton-thick population and a very large reflection component ($R \simeq 2$) at all luminosities can also reproduce the CXB (Akylas et al. 2012; Aird et al. 2015). The Ricci et al. (2017) *Swift*-BAT 70-month sample has a median biased R value (biased toward high R) of 1.3 and a bias-corrected median R value of 0.53. Zappacosta et al. (2018) analyzed *NuSTAR* spectra of 63 sources and found $\langle R \rangle = 0.43$ and an interquartile range of 0.06−1.5. Therefore, observed R values are smaller than the value required to support small Compton-thick number densities. Therefore, these densities may indeed be very high. In a future work, we will explore the consequences of these space densities on SMBH mass function.

This work and U14 fit overall AGN number counts better than A15 and B15, which serves as a cross-validation for the higher proportion of Compton-thick objects. Currently, our model is the only XLF that consistently fits all existing constraints.

The second most important result from our work is that we demonstrate, with examples, that the parameter space of AGN spectra that can reasonably reproduce the CXB is limited. Spectral Sets 2 and 3 are examples of a combination of spectral parameters that do not consistently reproduce all parts of the CXB for any underlying XLF, and Spectral Set 4 is an example where the CXB can be reproduced reasonably, but number counts, in this case Compton-thick number counts, remain largely underestimated.

The results for Spectral Set 1 and Spectral Set 5 are very similar, but the two spectral sets are not, as shown in Figure 7, and therefore the XLFs that produce the results are also different. We find that Spectral Set 5 is a better fit to the CXB (Figure 11 and Table 5) and to the R15 intrinsic absorption function (Figure 10). The similarity between Spectral Sets 1 and 5, as shown in Figure 7, is that despite the different Γ and E_C values, they are both considerably lower at $E > 20$ keV than Spectral Sets 2, 3, and 4. This steep decline of the intrinsic power law seems to be a necessary condition to reproduce the CXB spectra and can be caused by a higher photon index or a lower cutoff energy. Observed AGN spectra indicate that cutoff energies are ubiquitous (Ricci et al. 2017), and in our analysis we find that a high photon index cannot be used to completely replace cutoff energies; the B15 XLF originally did not have a cutoff energy but had a high photon index (1.95). However, this approach makes the CXB constant from $E \simeq 30$ keV for all 1000 XLF predictions, consequently heavily overestimating the CXB at $E > 30$ keV (results of that fit are shown in Table 5).

Spectral Set 1 slightly underestimates the CXB at $E > 60$ keV. Spectral Set 5 produces a better fit and can possibly be further improved with less steep spectra, i.e., with a lower Γ value than 1.96. The best distribution of Γ, assuming the bias-corrected cutoff energy from the *Swift*-BAT 70-month sample (200 keV) and reflection scaling factors, should have a $\langle \Gamma \rangle$ between 1.8 and 1.96.

Finally, it must be noted that the upcoming *Swift*-BAT 105-month spectral measurements and the increasing *NuSTAR* data will contribute to better constraints on AGN spectra.

8. Summary

We find that the most recent population synthesis models do not fit all the current X-ray observational constraints. We generated a comprehensive population synthesis model for black hole growth, consisting of AGN number densities as a function of luminosity, redshift, and absorbing column density, which simultaneously accounts for the number counts and Compton-thick fractions in X-ray surveys spanning a range of depths and areas (corresponding to a wide range in luminosity and redshifts) and the integrated spectrum of the CXB. Specifically, given a set of input AGN spectra, we employed a neural network to find space densities that fit the X-ray background and then identified the best-fit model according to fits to the observed number counts and Compton-thick fractions. We took observational uncertainties in AGN spectra into account.

We find that the new population synthesis model predicts a much higher space density of Compton-thick objects, especially at high luminosities, than prior luminosity functions. This population matches observed Compton-thick number counts and fractions from *XMM-Newton*, *Chandra*, *Swift*-BAT, and *NuSTAR* surveys and predicts that intrinsically $50\% \pm 9\%$ ($56\% \pm 7\%$) of all AGNs within $z \simeq 0.1$ (1.0) are Compton-thick. We also show that AGN spectral assumptions affect the shape of the predicted X-ray background in population synthesis models, and certain spectral combinations do not suitably reproduce it for any space densities of AGNs.

Our XLF is available as a 3D `numpy` array, with instructions on calculating space densities using a 3D grid interpolator. It can be downloaded from Bitbucket[13] and is archived in Zenodo (doi:10.5281/zenodo.2522799).

This material is based on work supported by the National Science Foundation under grant no. AST-1715512 and Yale University. E.T. acknowledges support from FONDECYT Regular 1160999, CONICYT PIA ACT172033, and Basal-CATA PFB-06/2007 and AFB170002 grants. T.A. wishes to thank her parents, M. A. Quayum and Shamim Ara Begum, her husband, Mehrab Bakhtiar, and her sisters, Arnita Tasnim and Raysa Tasnim, for their support. T.A. also wishes to thank Dr. Trey Ashton Belew for his help with multiprocessing and Dr. Lia Sartori for advice on X-ray spectra.

Software: `numpy` (Van Der Walt et al. 2011), `Astropy` (The Astropy Collaboration et al. 2018), `Matplotlib` (Hunter 2007), `Topcat` (Taylor 2005), XSPEC and PYXPSEC (Arnaud 1996), and `Vegas` (Lepage 1980). Parts of the neural network code was adapted from Nielsen (2015).

Appendix A
Initial Approach: Updating $N_{\rm H}$ Function

Here we provide a detailed background to the U14 absorption function and how it was updated using R15 results. The first step in formulating the U14 $N_{\rm H}$ distribution was to find the fraction of Compton-thin objects (ψ)—$\log(N_{\rm H}/{\rm cm}^{-2}) = 22$–24—among all objects with $\log(N_{\rm H}/{\rm cm}^{-2}) < 24$. The function itself was normalized within $\log(N_{\rm H}/{\rm cm}^{-2}) = 20$–24, as there were too few Compton-thick objects securely identified in the three fields to adequately formulate the $\log(N_{\rm H}/{\rm cm}^{-2}) > 24$ region. As a result, the number/fraction of Compton-thick sources was essentially a free parameter. The fraction of Compton-thin objects is dependent on luminosity and redshift, $\psi(L_X, z)$, and is best constrained at $\log(L_X/{\rm erg\,s}^{-1}) = 43.75$ in the local universe using *Swift*-BAT data. Then, on the basis of Treister & Urry (2006) and Hasinger (2008) and independent U14 analysis, a redshift dependence is added to ψ ($L_X = 43.75$, $z = 0$) as follows:

$$\begin{cases}(1+z)^{0.48} & z < 2.0\\ (1+2)^{0.48} & z \geqslant 2.0\end{cases}. \quad (1)$$

Therefore, the complete luminosity- and redshift-dependent absorbed fraction is $\psi(L_X, z) = \psi\ (L_X = 43.75, z) - 0.24 \times (\log L_X - 43.75)$, with forced upper and lower bounds at 0.84 and 0.2, respectively. These limits are imposed based on U14 analysis of *Swift*-BAT data ($\psi_{\rm max} = 0.84$) and Burlon et al. (2011) ($\psi_{\rm min} = 0.2$).

[13] https://bitbucket.org/tonimatas/xlf-final-result/downloads/

The absorption function is described in detail in Section 3.1 of U14. The data allowed the unabsorbed and Compton-thin bins to be much more robustly constrained than Compton-thick bins. Therefore, U14 normalized the absorption function in the $\log(N_{\rm H}/{\rm cm}^{-2}) = 20$–24 bins and assumed the same number of Compton-thick sources (at each luminosity and redshift) as the total number of Compton-thin sources, uniformly spread over $\log(N_{\rm H}/{\rm cm}^{-2}) = 24$–26 bins. We replaced the local absorption function using the R15 absorption function, as it is based on the *Swift*-BAT 70-month survey, which updated the older 9-month survey.

The R15 intrinsic $N_{\rm H}$ function is normalized to one between $\log(N_{\rm H}/{\rm cm}^{-2}) = 20$ and 25 in two 14–195 keV luminosity bins, for a $z < 0.3$ sample with median $z \sim 0.055$. These luminosity boundaries translate to different 2–10 keV luminosities, depending on the spectrum we assume. We convert $\log(L_{14-195}/{\rm erg\,s}^{-1}) = 43.7$ to $\log(L_{2-10}/{\rm erg\,s}^{-1}) = 43.58$ assuming $\Gamma = 1.76$ and a cutoff energy of 60 keV, which are median spectral parameters for the *Swift*-BAT 70-month sample (Ricci et al. 2017).

In our initial attempt, we renormalized R15 in the $\log(N_{\rm H}/{\rm cm}^{-2}) = 20$–24 bins. We kept the total number of U14 objects in $\log N_{\rm H}/{\rm cm}^2 < 24$ unchanged and only redistributed objects within adjacent bins—which is sufficient to reproduce the R15 absorption function (as shown in Figure 10). However, we add more objects in the Compton-thick bins, according to the R15 fraction. Then, we incorporated luminosity dependence into $\psi(L_x, z)$, by taking the R15 fractions as flat for the two luminosity bins ($\log(L_{2-10}/{\rm erg\,s}^{-1}) < 43.58$ and $\log(L_{2-10}/{\rm erg\,s}^{-1}) \geqslant 43.58$).

The luminosity and redshift dependence of the absorbed fraction follows (z increases to a maximum value of 2)

$$\psi(L_x, z) = \begin{cases}(0.68 \pm 0.04)(1+z)^{0.48\pm0.05}, & L_{2-10} < 43.58\\ (0.50 \pm 0.04)(1+z)^{0.48\pm0.05}, & L_{2-10} \geqslant 43.58.\end{cases} \quad (2)$$

Following U14, we use a maximum and minimum ψ of 0.84 and 0.2, respectively. The updated $N_{\rm H}$ function is normalized in the $\log(N_{\rm H}/{\rm cm}^{-2}) = 20$–24 region. The ratio of number of objects in the $\log(N_{\rm H}/{\rm cm}^{-2}) = 23$–24 bin to that in the $\log(N_{\rm H}/{\rm cm}^{-2}) = 22$–23 bin, the ϵ parameter from U14, is slightly lower in the R15 model than in U14, but it is within the range reported in the literature—between 1.3 and 1.7 (Risaliti et al. 1999; Tueller et al. 2008; Vasudevan et al. 2013). In the R15 $\log(L_{2-10}/{\rm erg\,s}^{-1}) < 43.6$ bin, $\epsilon = 1.3205 \pm 0.17469$, and in the $L_{2-10} \geqslant 43.6$ bin, $\epsilon = 1.4885 \pm 0.24079$. U14 uses a fixed value for ϵ. Overall, the absorption function is as follows.

For $\log(L_{2-10}/{\rm erg\,s}^{-1}) < 43.58$ (in the following equations, $\psi = \psi(L_x, z)$ as shown in Equation (2)),

$$f(L_x, z; N_{\rm H}) = \begin{cases}(0.74 \pm 0.06) \times (1-\psi) & [20 \leqslant \log N_{\rm H} < 21]\\ (0.26 \pm 0.06) \times (1-\psi) & [21 \leqslant \log N_{\rm H} < 22]\\ \dfrac{1}{1+\epsilon}\psi & [22 \leqslant \log N_{\rm H} < 23]\\ \dfrac{\epsilon}{1+\epsilon}\psi & [23 \leqslant \log N_{\rm H} < 24]\\ (0.69 \pm 0.15) \times \psi & [24 \leqslant \log N_{\rm H} < 26]\end{cases}. \quad (3)$$

For $\log[L_{2-10}/\mathrm{erg\,s^{-1}}] \geqslant 43.58$,

$$f(L_x, z; N_{\rm H}) = \begin{cases} (0.77 \pm 0.05) \times (1-\psi) & [20 \leqslant \log N_{\rm H} < 21] \\ (0.23 \pm 0.05) \times (1-\psi) & [21 \leqslant \log N_{\rm H} < 22] \\ \dfrac{1}{1+\epsilon}\psi & [22 \leqslant \log N_{\rm H} < 23] \\ \dfrac{\epsilon}{1+\epsilon}\psi & [23 \leqslant \log N_{\rm H} < 24] \\ (0.52 \pm 0.08) \times \psi & [24 \leqslant \log N_{\rm H} < 26]. \end{cases} \quad (4)$$

Similar to U14, we assumed the Compton-thick absorption function to be flat over the log $(N_{\rm H}/\mathrm{cm^{-2}}) = 24$–$26$ range. After editing the U14 XLF with the R15 absorption function (U14+R15), we find that number counts in the 0.5–2 keV and 2–7 keV bands from the CDFS 7 Ms catalog are still underestimated by $\simeq$40% at the faintest flux ends, and the Compton-thick number counts remain underestimated. We also tried adding the luminosity dependence of ψ found in Barger et al. (2005), where it linearly decreases from 0.8 to 0.2 between log $(L_{2-10}/\mathrm{erg\,s^{-1}}) = 42.0$ and 46.0. This relationship can be incorporated without violating R15, if we relax the linear fraction to vary from 0.7 to 0.3 for log $(L_{2-10}/\mathrm{erg\,s^{-1}})$ of 42.0 to 46.0. This made the absorption function more complicated but did not improve results, so we neglected it. We used the U14 XLF with a modified absorption function, as described in Equations (2)–(4), as input into the neural network.

Appendix B
Back-propagation Algorithm

Here we explain how a back-propagation algorithm is used to determine our best-fit population synthesis model. In neural networks, a layer of input neurons receives input broken down into chunks; for instance, a handwriting recognition network would take information about black-to-white ratio of pixels for different parts of the image for different input neurons. This input vector of the ratio would be called $\boldsymbol{x}$—where x_j is the ratio of black to white ink in the jth input neuron. The inputs from all the layers sum up and reach each neuron in a new layer of neurons. Each of these neurons in the new layer has different weights associated with the neurons in the previous layer, such that, for neuron i in layer 2, the output "activation" value a_i is

$$a_i = \begin{cases} 0, & \boldsymbol{w}\cdot\boldsymbol{x} < \mathrm{threshold}_i \\ 1, & \boldsymbol{w}\cdot\boldsymbol{x} \geqslant \mathrm{threshold}_i \end{cases}. \quad (5)$$

Here $\boldsymbol{w}$ is the vector of weights associated with each neuron in the input layer, and $\mathrm{threshold}_i$ is the bias associated with neuron i in the new layer (mathematically, bias $= -$threshold). If this $\mathrm{threshold}_i$ value is exceeded by the dot product of the input and weights, then this neuron is activated and sends an input signal of 1 to the next layer, and if it falls below the threshold, this neuron sends a 0 to the next layer. Usually a more sophisticated function is used to calculate a_i that outputs a range of values between 0 and 1, rather than just the binary values. A sigmoid function $(\sigma(z) = \frac{1}{1+e^{-z}})$ is a commonly used activation function because its derivatives have nice properties, but we cannot do an analytic differentiation with the CXB, so the sigmoid function is not used in our neural network.

A normal neural network, such as a handwriting recognition network, is composed of a series of layers of neurons, each neuron with an array of weights associated with each neuron in the previous layer, and a bias. All these weights and biases are readjusted according to each input in the training data set, so that the final set of weights and biases can predict which handwritten letter is seen using the ratio of black and white pixels in different parts of the image. The readjustment process is done by optimizing a cost function, which is

$$C(w) \propto \Sigma_x ||y(x) - a(w)||^2, \quad (6)$$

where w is the collection of all weights in the network, y is the final output, and a is the activation. The weights are updated using gradient descent (see comprehensive explanation by Nielsen 2015). In this work, the activation function is the predicted X-ray background, and the cost function is the difference between the observed X-ray background and the model predictions, as shown in Figure 6:

$$C(w) = \frac{1}{2n}\Sigma_E ||\mathrm{CXB_{obs}}(E) - \mathrm{CXB_{model}}(E, w)||^2, \quad (7)$$

where E is the energy for each CXB data point, and $\mathrm{CXB_{model}}$ is evaluated using the integral

$$\mathrm{CXB_{model}}(E, w) \propto \int_{z_{\rm min}}^{z_{\rm max}} \int_{L_{2-10,\,\rm min}}^{L_{2-10,\,\rm max}} \int_{\log N_{\rm H,min}}^{\log N_{\rm H,max}} \times \mathrm{XLF}(z, L_{2-10}, \log N_{\rm H}|w_1,\ldots,w_{15}) \times \mathrm{Spectra}(E(1+z))\, dz\, dL_{2-10}\, d\log N_{\rm H}. \quad (8)$$

After calculating cost C, the derivative of C, $\partial C(w_i)/\partial w_i$, is calculated numerically for each weight:

$$\frac{\partial C(w_i)}{\partial w_i} = \frac{C(w_1,\ldots,w_i+\partial w_i,\ldots) - C(w_1,\ldots,w_i,\ldots)}{\partial w_i}, \quad (9)$$

where $C(w_1, \ldots, w_i, \ldots)$ is the cost for the current step. The weights are then updated so that the cost function is minimized:

$$w_i \mapsto w_i' = w_i - \eta\frac{\partial C(w_i)}{\partial w_i}, \quad (10)$$

where η is the step size. Using this method, we readjust weights in such a way that the fit to the CXB improves with each iteration. We present our best solution as a new XLF in Section 6.

Appendix C
Discrepancy In CXB Plot

In U14, the photon index for absorbed objects is $\langle\Gamma\rangle = 1.84$ with a dispersion of $\Gamma_\mu = 0.15$, and the photon index of unabsorbed objects is $\langle\Gamma\rangle = 1.94$ with a dispersion of $\Gamma_\mu = 0.09$. For A15, the photon index for all AGNs is $\langle\Gamma\rangle = 1.9$ with a dispersion of $\Gamma_\mu = 0.2$. We find that using a Gaussian distribution of photon indices with these dispersions produces the CXB shown in Figure 11. However, if we keep the photon index constant at $\langle\Gamma\rangle$ values instead of using a distribution, we recover the CXB published in U14 and A15. The result of not using a distribution for A15 and U14 is shown in Figure 18. In B15, no CXB was plotted for the model, so we use a prescribed distribution of photon index in B15 in both Figures 11 and 18. Here we show the 10th–90th percentile predictions of the constant slope and constant value predictions by B15.

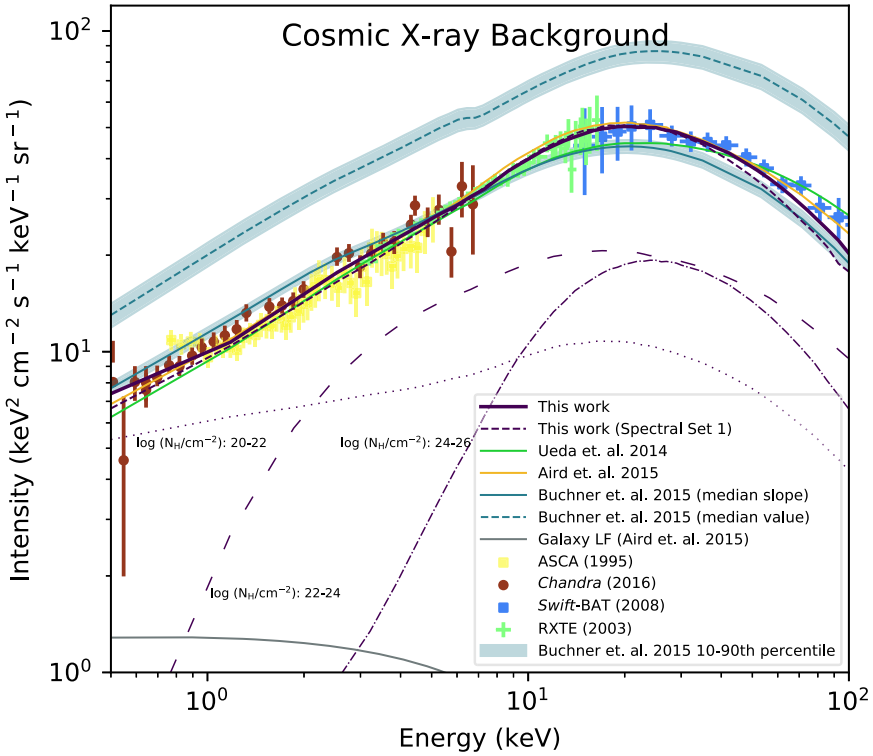

Figure 18. Empirical X-ray background (CXB) from *Chandra* COSMOS (red circles), *ASCA* (yellow squares), *RXTE* (green crosses), and *Swift*-BAT (blue squares). The models are this work (solid purple line), Spectral Set 1 results (dotted purple line, also from this work), U14 (light-green line), A15 (yellow line), the B15 median of constant slope prior (gray solid line), and the B15 median of constant value prior (gray dashed line). We added a cutoff energy of 200 keV to the B15 spectral model to bring the XLF in better agreement with the CXB at higher energies. A galaxy contribution has been added to each CXB model prediction, according to the A15 galaxy luminosity function (black solid line). Total contributions to the CXB from three absorption bins for this work are also shown: log (N_H/cm^{-2}) = 20–22 is shown by the dotted purple line, log (N_H/cm^{-2}) = 22–24 is shown by the sparsely dashed purple line, and log (N_H/cm^{-2}) = 24–26 is shown by the the dotted-dashed purple line. In this plot, we remove the dispersion in photon indices for the U14 and A15 models, which brings our calculations in agreement with published results in U14 and A15. We also show the 10th–90th percentile CXB predictions (gray shaded region) for the B15 constant slope and constant value assumptions. We ignore the constant value assumption in the number count plots, as the constant slope prediction is a closer match to X-ray background data.

ORCID iDs

Tonima Tasnim Ananna https://orcid.org/0000-0001-8211-3807
Ezequiel Treister https://orcid.org/0000-0001-7568-6412
C. Megan Urry https://orcid.org/0000-0002-0745-9792
C. Ricci https://orcid.org/0000-0001-5231-2645
Allison Kirkpatrick https://orcid.org/0000-0002-1306-1545
Stephanie LaMassa https://orcid.org/0000-0002-5907-3330
Johannes Buchner https://orcid.org/0000-0003-0426-6634
Stefano Marchesi https://orcid.org/0000-0001-5544-0749

References

Aird, J., Alexander, D. M., Ballantyne, D. R., et al. 2015, ApJ, 815, 66
Aird, J., Coil, A. L., Georgakakis, A., et al. 2015, MNRAS, 451, 1892
Aird, J., Nandra, K., Laird, E. S., et al. 2010, MNRAS, 401, 2531
Ajello, M., Greiner, J., Sato, G., et al. 2008, ApJ, 689, 666
Akiyama, M., Ueda, Y., Ohta, K., Takahashi, T., & Yamada, T. 2003, ApJS, 148, 275
Akylas, A., Georgakakis, A., Georgantopoulos, I., Brightman, M., & Nandra, K. 2012, A&A, 546, A98
Alexander, D. M., Stern, D., Del Moro, A., et al. 2013, ApJ, 773, 125
Ananna, T. T., Salvato, M., LaMassa, S., et al. 2017, ApJ, 850, 66
Arnaud, K. A. 1996, in ASP Conf. Ser. 101, Astronomical Data Analysis Software and Systems V, ed. G. H. Jacoby & J. Barnes (San Francisco, CA: ASP), 17
Ballantyne, D. R., Draper, A. R., Madsen, K. K., Rigby, J. R., & Treister, E. 2011, ApJ, 736, 56
Baloković, M., Brightman, M., Harrison, F. A., et al. 2018, ApJ, 854, 42
Barger, A. J., Cowie, L. L., Mushotzky, R. F., et al. 2005, AJ, 129, 578
Barthelmy, S. D., Barbier, L. M., Cummings, J. R., et al. 2005, SSRv, 120, 143
Boyle, B. J., Griffiths, R. E., Shanks, T., Stewart, G. C., & Georgantopoulos, I. 1993, MNRAS, 260, 49
Boyle, B. J., & Terlevich, R. J. 1998, MNRAS, 293, L49
Brandt, W. N., & Hasinger, G. 2005, ARA&A, 43, 827
Brightman, M., & Nandra, K. 2011, MNRAS, 413, 1206
Buchner, J., Georgakakis, A., Nandra, K., et al. 2014, A&A, 564, A125
Buchner, J., Georgakakis, A., Nandra, K., et al. 2015, ApJ, 802, 89
Burlon, D., Ajello, M., Greiner, J., et al. 2011, ApJ, 728, 58
Burrows, D. N., Hill, J. E., Nousek, J. A., et al. 2005, SSRv, 120, 165
Cappelluti, N., Hasinger, G., Brusa, M., et al. 2007, ApJS, 172, 341
Cappelluti, N., Li, Y., Ricarte, A., et al. 2017, ApJ, 837, 19
Cardamone, C. N., Urry, C. M., Damen, M., et al. 2008, ApJ, 680, 130
Chen, C.-T. J., Hickox, R. C., Alberts, S., et al. 2015, ApJ, 802, 50
Civano, F., Hickox, R. C., Puccetti, S., et al. 2015, ApJ, 808, 185
Clements, D. L., Sutherland, W. J., McMahon, R. G., & Saunders, W. 1996, MNRAS, 279, 477
Comastri, A., Setti, G., Zamorani, G., & Hasinger, G. 1995, A&A, 296, 1
Cowie, L. L., Barger, A. J., Bautz, M. W., Brandt, W. N., & Garmire, G. P. 2003, ApJL, 584, L57
Del Moro, A., Alexander, D. M., Bauer, F. E., et al. 2016, MNRAS, 456, 2105
Di Matteo, T., Springel, V., & Hernquist, L. 2005, Natur, 433, 604
Donley, J. L., Koekemoer, A. M., Brusa, M., et al. 2012, ApJ, 748, 142
Elvis, M., Civano, F., Vignali, C., et al. 2009, ApJS, 184, 158
Ferrarese, L., & Ford, H. 2005, SSRv, 116, 523
Ferrarese, L., & Merritt, D. 2000, ApJL, 539, L9
Fiore, F., Feruglio, C., Shankar, F., et al. 2017, A&A, 601, A143
Fiore, F., Grazian, A., Santini, P., et al. 2008, ApJ, 672, 94
Gandhi, P., & Fabian, A. C. 2003, MNRAS, 339, 1095
Gebhardt, K., Bender, R., Bower, G., et al. 2000, ApJL, 539, L13
Gehrels, N., Chincarini, G., Giommi, P., et al. 2004, ApJ, 611, 1005
Gendreau, K. C., Mushotzky, R., Fabian, A. C., et al. 1995, PASJ, 47, L5

Giacconi, R., Zirm, A., Wang, J., et al. 2002, ApJS, 139, 369
Gilli, R., Comastri, A., & Hasinger, G. 2007, A&A, 463, 79
Gilli, R., Salvati, M., & Hasinger, G. 2001, A&A, 366, 407
Harrison, F. A., Aird, J., Civano, F., et al. 2016, ApJ, 831, 185
Harrison, F. A., Craig, W. W., Christensen, F. E., et al. 2013, ApJ, 770, 103
Hasinger, G. 2008, A&A, 490, 905
Hopkins, P. F., Hernquist, L., Cox, T. J., et al. 2006, ApJS, 163, 1
Hunter, J. D. 2007, CSE, 9, 90
Jiménez-Vicente, J., Mediavilla, E., Kochanek, C. S., et al. 2014, ApJ, 783, 47
Jones, L. R., McHardy, I. M., Merrifield, M. R., et al. 1997, MNRAS, 285, 547
Kim, M., Kim, D.-W., Wilkes, B. J., et al. 2007, ApJS, 169, 401
Kirkpatrick, A., Pope, A., Sajina, A., et al. 2015, ApJ, 814, 9
Kormendy, J., & Gebhardt, K. 2001, in AIP Conf. Ser. 586, 20th Texas Symp. Relativistic Astrophysics, ed. J. C. Wheeler & H. Martel (Melville, NY: AIP), 363
Kormendy, J., & Ho, L. C. 2013, ARA&A, 51, 511
LaMassa, S. M., Urry, C. M., Cappelluti, N., et al. 2013a, MNRAS, 436, 3581
LaMassa, S. M., Urry, C. M., Cappelluti, N., et al. 2016, ApJ, 817, 172
LaMassa, S. M., Urry, C. M., Glikman, E., et al. 2013b, MNRAS, 432, 1351
Lansbury, G. B., Alexander, D. M., Aird, J., et al. 2017, ApJ, 846, 20
Lansbury, G. B., Stern, D., Aird, J., et al. 2017, ApJ, 836, 99
Lanzuisi, G., Civano, F., Marchesi, S., et al. 2018, MNRAS, 480, 2578
Lehmer, B. D., Brandt, W. N., Alexander, D. M., et al. 2005, ApJS, 161, 21
Lehmer, B. D., Tyler, J. B., Hornschemeier, A. E., et al. 2015, ApJ, 806, 126
Lehmer, B. D., Xue, Y. Q., Brandt, W. N., et al. 2012, ApJ, 752, 46
Lepage, G. P. 1980, VEGAS: An Adaptive Multi-dimensional Integration Routine, Tech. Rep. CLNS-80/447 (Ithaca, NY: Newman Lab. Nuclear Studies)
Luo, B., Brandt, W. N., Xue, Y. Q., et al. 2017, ApJS, 228, 2
Maccacaro, T., della Ceca, R., Gioia, I. M., et al. 1991, ApJ, 374, 117
Magdziarz, P., & Zdziarski, A. A. 1995, MNRAS, 273, 837
Magorrian, J., Tremaine, S., Richstone, D., et al. 1998, AJ, 115, 2285
Malizia, A., Molina, M., Bassani, L., et al. 2014, ApJL, 782, L25
Martín-Navarro, I., Brodie, J. P., Romanowsky, A. J., Ruiz-Lara, T., & van de Ven, G. 2018, Natur, 553, 307
Masini, A., Civano, F., Comastri, A., et al. 2018, ApJS, 235, 17
Masini, A., Comastri, A., Baloković, M., et al. 2016, A&A, 589, A59
Mateos, S., Warwick, R. S., Carrera, F. J., et al. 2008, A&A, 492, 51
Matt, G. 2001, in AIPC Conf. Ser. 599, X-ray Astronomy: Stellar Endpoints, AGN, and the Diffuse X-ray Background, ed. N. White, G. Malaguti, & G. G. C. Palumbo (Melville, NY: AIP), 209
Matt, G., Fabian, A. C., Guainazzi, M., et al. 2000, MNRAS, 318, 173
Mendez, A. J., Coil, A. L., Aird, J., et al. 2013, ApJ, 770, 40
Merloni, A., Bongiorno, A., Bolzonella, M., et al. 2010, ApJ, 708, 137
Merritt, D., & Ferrarese, L. 2001, ApJ, 547, 140
Miyaji, T., Hasinger, G., & Schmidt, M. 2000, A&A, 353, 25
Moretti, A., Pagani, C., Cusumano, G., et al. 2009, A&A, 493, 501
Mullaney, J. R., Del-Moro, A., Aird, J., et al. 2015, ApJ, 808, 184
Nandra, K. 2006, MNRAS, 368, L62
Nandra, K., O'Neill, P. M., George, I. M., & Reeves, J. N. 2007, MNRAS, 382, 194
Nandra, K., & Pounds, K. A. 1994, MNRAS, 268, 405
Nenkova, M., Ivezić, Ž, & Elitzur, M. 2002, ApJL, 570, L9
Nielsen, M. A. 2015, Nielsen, Neural Networks and Deep Learning (San Francisco, CA: Determination Press)
Page, M. J., Mason, K. O., McHardy, I. M., Jones, L. R., & Carrera, F. J. 1997, MNRAS, 291, 324
Persic, M., & Rephaeli, Y. 2002, A&A, 382, 843
Persic, M., & Rephaeli, Y. 2003, A&A, 399, 9
Petrucci, P. O., Haardt, F., Maraschi, L., et al. 2001, ApJ, 556, 716
Pierre, M., Pacaud, F., Adami, C., et al. 2016, A&A, 592, A1
Ranalli, P., Comastri, A., Vignali, C., et al. 2013, A&A, 555, A42
Revnivtsev, M., Gilfanov, M., Sunyaev, R., Jahoda, K., & Markwardt, C. 2003, A&A, 411, 329
Ricci, C., Bauer, F. E., Treister, E., et al. 2017, MNRAS, 468, 1273
Ricci, C., Trakhtenbrot, B., Koss, M. J., et al. 2017, ApJS, 233, 17
Ricci, C., Ueda, Y., Koss, M. J., et al. 2015, ApJL, 815, L13
Richstone, D., Ajhar, E. A., Bender, R., et al. 1998, Natur, 395, A14
Risaliti, G., Maiolino, R., & Salvati, M. 1999, ApJ, 522, 157
Taylor, M. B. 2005, in ASP Conf. Ser. 347, Astronomical Data Analysis Software and Systems XIV, ed. P. Shopbell, M. Britton, & R. Ebert (San Francisco, CA: ASP), 29
The Astropy Collaboration, Price-Whelan, A. M., Sipőcz, B. M., et al. 2018, AJ, 156, 123
Treister, E., & Urry, C. M. 2006, ApJL, 652, L79
Treister, E., Urry, C. M., Schawinski, K., Cardamone, C. N., & Sanders, D. B. 2010, ApJL, 722, L238
Treister, E., Urry, C. M., & Virani, S. 2009, ApJ, 696, 110
Tueller, J., Mushotzky, R. F., Barthelmy, S., et al. 2008, ApJ, 681, 113
Ueda, Y., Akiyama, M., Hasinger, G., Miyaji, T., & Watson, M. G. 2014, ApJ, 786, 104
Ueda, Y., Akiyama, M., Ohta, K., & Miyaji, T. 2003, ApJ, 598, 886
Ueda, Y., Ishisaki, Y., Takahashi, T., Makishima, K., & Ohashi, T. 2001, ApJS, 133, 1
Ueda, Y., Watson, M. G., Stewart, I. M., et al. 2008, ApJS, 179, 124
Van Der Walt, S., Colbert, S. C., & Varoquaux, G. 2011, CSE, 13, 22
Vasudevan, R. V., Brandt, W. N., Mushotzky, R. F., et al. 2013, ApJ, 763, 111
Weisskopf, M. C., Brinkman, B., Canizares, C., et al. 2002, PASP, 114, 1
Wik, D. R., Lehmer, B. D., Hornschemeier, A. E., et al. 2014, ApJ, 797, 79
Xue, Y. Q., Wang, S. X., Brandt, W. N., et al. 2012, ApJ, 758, 129
Yukita, M., Hornschemeier, A. E., Lehmer, B. D., et al. 2016, ApJ, 824, 107
Zappacosta, L., Comastri, A., Civano, F., et al. 2018, ApJ, 854, 33
Zdziarski, A. A., Lubiński, P., & Smith, D. A. 1999, MNRAS, 303, L11
Zdziarski, A. A., Poutanen, J., & Johnson, W. N. 2000, ApJ, 542, 703